A ship-borne wave gauge using GNSS Interferometric Reflectometry

朱，鏡橋
九州大学大学院総合理工学府総合理工学専攻地球環境理工学メジャー

https://hdl.handle.net/2324/7182201

出版情報：九州大学，2022，修士，修士
バージョン：
権利関係：

令和４年度

九州大学大学院総合理工学府

総合理工学専攻地球環境理工学メジャー修士論文

A ship-borne wave gauge using GNSS Interferometric Reflectometry

氏　　　名 朱鏡橋　(Jingqiao Zhu)

指導教員名 市川　香 (Kaoru Ichikawa)

A ship-borne wave gauge using GNSS Interferometric Reflectometry

Abstract: For wide coverage and good observation frequency for the significant wave height (SWH) of measurement, the observation can be made ship-borne using GNSS interferometric reflectometry. If the water surface vertically moves by waves, the path delay changes, and the phase delays variate, which is recognized by SNR received from the single antenna. The SNR curve includes lots of high-frequency variations, since every time when the phase delay becomes zero, SNR becomes local maximum. Therefore, the number of high-frequency variations would correspond to the number of interference stripes with every wavelength of GNSS. The relationship between this number and the SWH could be established by counting the number crossing the value lines and the SNR curve. With help of the single-frequency wave and multi-frequency wave models of the ISSC Spectrum, we can estimate the SWH after determining the wave period by ACF. The fundamental pattern, which is more numbers crossing the larger SWH becomes, could be proved in three different sea states of the Tsushima Strait.

Keywords: ship-borne; significant wave height; GNSS-IR; wave period; SNR

TABLE OF CONTENTS

CHAPTER 1: Introduction 1
1.1 Background and Purpose 1
1.2 GNSS-R (Global Navigation Satellite Systems-Reflectometry) 3
1.2.1 Dual antenna observation mode 3
1.2.2 Single-antenna observation mode 6
CHAPTER 2: Methodology 8
2.1 The GNSS-IR for measurement 8
2.2 The flow of the experiment 12
2.2.1 Satellite vision and the pre-processing 12
2.2.2 the Indexes of rapidness of SNR changes 13
2.2.3 the wave period estimation 16
2.2.5 Build the model and SWH estimation 17
CHAPTER 3: Result 18
3.1 wave simulation 18
3.1.1 Single-frequency wave simulation 18
3.1.2 Dependency of the ratio(r) the distance (H) 22
3.1.3 Dependency of the elevation angles (θ) and wavelength of GNSS (λ) 23
3.1.4 Multi-frequency wave simulation with ISSC Spectrum 24
3.2 Validation 29
3.2.1 Observation area and SNR data on shipborne 29
3.2.2 Calm sea state 32
3.2.3 Standard sea state 35
3.2.4 Rougher sea state 38
3.2.5 Intercomparison of results 41
CHAPTER 4: Discussion and Conclusion 43
4.1 Discussion 43
4.2 Conclusion 47
Reference: 48

CHAPTER 1: Introduction

1.1 Background and Purpose

Monitoring the ocean, provides fundamental data for marine operations, meteorology, and oceanographic research. It enables accurate forecasting of marine phenomena closely related to human activities, makes marine transportation and resource development operations safe and effective, helps researchers study marine phenomena well, and builds accurate marine models.

The wave height of a surface is the difference between the elevations of a crest and a neighboring trough in fluid dynamics [1]. At sea, the term significant wave height is used as a means to introduce a well-defined and standardized statistic to denote the characteristic height of the random waves in a sea state, including wind, sea, and swell. In physical oceanography, the significant wave height (SWH, HTSGW[2] or Hs) is defined traditionally as the mean wave height (trough to crest) of the highest third of the waves ($H_{1/3}$). Significant wave height is one of the most important parameters for characterizing the ocean surface and is therefore monitored by the offshore industry for their daily operation.

Because waves influence so many processes and operations at sea, many techniques have been invented for measuring waves. The most common devices are Tide gauges, buoys, Satellite Altimeters, Synthetic Aperture Radars (SAR).

For ordinary wave observations, Tide gauges and buoys are commonly used. Gauges may be mounted on platforms or on the seafloor in shallow water. Many different types of sensors are used to measure the wave height or subsurface pressure related to wave height. Sound, infrared beams, and radio waves can be used to determine the distance from the sensor to the sea surface provided the sensor can be mounted on a stable platform that does not interfere with the waves. Some kinds of buoys are designed to measure wave heights with an accelerometer in waters where offshore construction projects and ocean surveys are conducted. Tide gauges and buoys can provide continuous observation for the significant wave height, wave period, and wave direction. But their locations are limited, and the data is only relevant to operations conducted within their immediate vicinity.

The satellite altimeters used to measure surface geostrophic currents also measure wave height. Another common instrument is Synthetic Aperture Radar (SAR) sensor on satellites. It measures backscatter from the ocean surface and can be used to estimate wave height at very high spatial resolution (~10 m) relative to satellite altimetry. All of the above instruments measure wave heights by remote sensing, non-contact means. They have a large coverage observation and get the data easily. But their sampling intervals are too long.

If we make wave observations by many ships with more sensors, it has a good observation frequency and wide coverage. But it is not perfect, there exists the disadvantage that the wave could be created by the ship itself and will affect the observation. There could be some improvements if we choose the shipboard observations with GNSS-R. It can take over that disadvantage.

1.2 GNSS-R (Global Navigation Satellite Systems-Reflectometry)

GNSS-R (Global Navigation Satellite Systems-Reflectometry) involves making measurements from the reflections from the Earth of navigation signals from Global Navigation Satellite Systems such as GPS.it uses surface-reflected GNSS signals to infer information about the Earth's surface. The reflected GNSS signals act as a bistatic remote sensing radar that responds to changing surface conditions. research applications are found in many fields (Altimetry, Oceanography (Wave Height and Wind Speed), Cryosphere monitoring, Soil moisture monitoring)

The basic principle of GNSS-R altimetry is to measure the delay distance of the reflected signal relative to the direct signal and to obtain the height of the observation point relative to the sea surface by inversion of the geometric relationship between the antenna height and the delay distance. According to the different GNSS-R observation antenna devices, can be divided into single-antenna and dual-antenna observation modes. The single-antenna observation mode mainly uses the interference (IPT)[3]of direct and reflected signals to measure the physical parameters of the reflecting surface. Dual antennas obtain the time delay difference of the reflected signal relative to the direct signal through the cooperative processing of both of them.

1.2.1 Dual antenna observation mode

Martin-Neira proposed the concept of passive reflectometry and interferometry system (PARIS) in 1993 for ocean remote sensing applications using reflected signals from navigation satellites [4]. Inspired by that, in 1996 NASA researchers experimentally applied the dual-frequency GPS signals' seaward forward scattering coefficients for atmospheric ionospheric delay modeling [5].

Based on the PARIS concept, Martin-Neira and other researchers from the European Space Agency conducted an experiment on sea surface height measurement based on GNSS reflection signals in Amsterdam in 1997 and achieved remarkable results, demonstrating the effectiveness of GNSS-R inversion [6,7]. Since then, many foreign universities and research institutes have conducted a series of scientific studies and experiments on GNSS reflection signals, mainly for shore-based and airborne (including aircraft and airboats) to study the reception and processing of GNSS sea surface scattering signals. The inversions include sea surface height [8], significant wave height, and sea surface wind field [9,10].

The dominant method for shore-based GNSS-R surface altimetry is single-antenna or dual-antenna carrier phase altimetry. In the literature [7],[11], using the carrier phase information of the GPS reflected signal, the accuracy of the measurement can reach the centimeter level, and Kucwaj et al. proposed a method to estimate the high accuracy code delay of the reflected signal relative to the direct signal with the aid of Doppler and carrier phase information, and the accuracy of the measurement can reach the centimeter level [12]. A study on the measurement of sea surface height based on the carrier phase of GNSS reflected signals was also carried out at the Onsala Space Observatory (OSO), Sweden. By comparing the experimental results with the tide gauge data, the RMSE of the sea surface height measurements was 4.37 cm, and the coefficient of correlation with the tide gauge data was 0.93 [13]. In 2017, Kucwaj proposed a method for estimating the sea surface height by circular regression using the characteristic that the phase time series of the reflected signal varies periodically, and the accuracy of the measurement can reach centimeter level, and the accuracy will increase with the increasing of the signal-noise ratio (SNR) of the reflected signal [14].

Airborne GNSS-R surface altimetry is mainly based on dual antenna mode. In 2002, Lowe et al. conducted an airborne GNSS reflection signal carrier phase altimetry experiment, and the accuracy of the first experiment was 14 cm, and the accuracy of the second experiment was 5 cm [15]. Ruffini et al. used a low-altitude airborne platform to collect GPS reflections with wind speed of 10 m/s and significant wave height of 2 m. They also performed code phase tracking on the experimental data, and the inverse surface height accuracy reached the decimeter level with a spatial resolution of 20 km[16]. The literature [17] analyzed data from airborne tests conducted in Monterey Bay, California, and proposed three reflected signal arrival time tracking algorithms with a measurement accuracy of up to 0.6m. Cardellach et al. conducted a dual-antenna interferometric sea surface altimetry study, experimental demonstration, and performance analysis with an accuracy of about 22 cm [18]. Through airborne experiments, it was demonstrated that the GPS P(Y) sea surface altimetry based on semi-codeless technology can improve the accuracy by 1.4-2.4 times compared to GPS C/A [19].

Martin-Neira proposed the PARIS In-Orbit experiment in 2011 and described the GNSS-R-based interference processing technology. Instead of generating local code signals, this technique directly interferes with the direct and reflected signals after carrier stripping [20]. Park et al. investigated the problem of time delay difference in ocean altimetry using interferometric processing under a satellite-based platform and proposed a method that can overcome the disadvantage of correlation window time delay synchronization [21]. Using the Cramer-Rao boundary analysis method, the literature [22] gives the measurement accuracy of PARIS sea surface altimetry for L1, L5, E1, E5, and E6 signals, and the results show that the E5 signal can provide the best measurement accuracy. D'Addio et al. start by solving the finite pulse mirror point area limitation problem and propose.

The multi-visual technique of using the whole DDM for sea surface height detection can improve the measurement accuracy compared with the traditional measurement method [23]. The literature [24] describes the ³Cat-2 satellite-based scheme, which aims to process the reflected signal P(Y) code using a semi-codeless technique to achieve higher accuracy of sea surface altitude measurements.

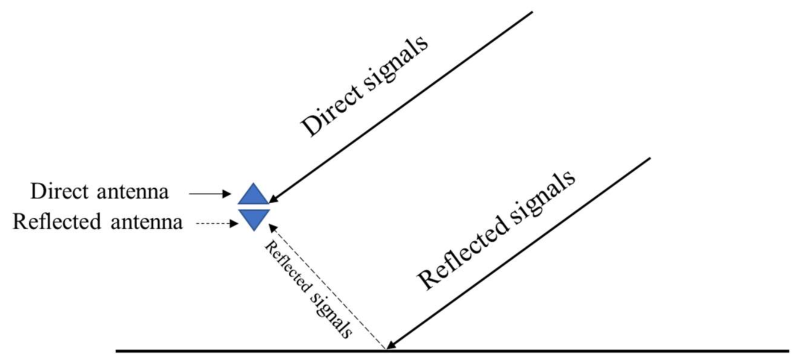

The dual antenna observation mode

Fig.1.1 Schematic concept of dual antenna observation mode

1.2.2 Single-antenna observation mode

Many studies have been carried out in China and abroad on single-antenna sea surface altimetry (SSA). Santamaría-Gómez et al. used the oscillation frequency of the direct inverse interference signal SNR to estimate the sea surface height and compared it with tidal data, and the MSE could reach 1.5cm[25]. The literature [26] proposed an improved method of single-antenna altimetry to improve the measurement accuracy and spatio-temporal resolution by considering the dynamic effect of sea surface height and multi-star fusion, and the results of a 3-month experiment showed that the correlation coefficient between sea surface height and tide level station data reached 0.97. Jin et al. conducted a study on single-antenna sea surface height measurement using BeiDou signals, and the obtained correlation coefficients between sea surface height and tide level station data were 0.83-0.91, and the RMSE was 0.6m [27].

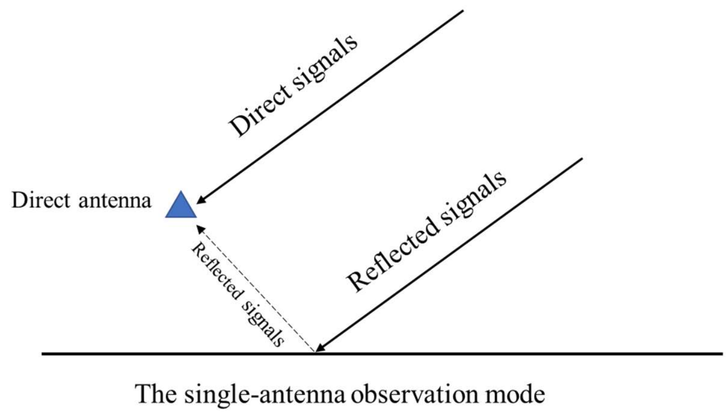

Fig.1.2 Schematic concept of single-antenna observation mode

In this study, we propose a method to measure significant wave heights using GNSS-R on the shipborne with the mode of the single antenna (GNSS-IR).

CHAPTER 2: Methodology

2.1 The GNSS-IR for measurement

In this study, we make observations in the mode of the single antenna, which is designed to receive both direct and reflected signals. In contrast to the dual-antenna observation mode, the SNR output from the receiver is used to infer the wave height. we don't need to develop a new receiver, and it has the features of simple operation and lower cost.

In terms of the type of data (SNR, signal-to-noise ratio) used, it has some advantages over other types of data, like Pseudorange data, Carrier phase data.

(1) Pseudorange data are usually used in the navigation community, but they are noisy and have their own complexities and large errors, also depend on clocks and the atmosphere and things like orbits.

(2) For carrier phase data, are used by geodesists and surveyors and are complicated in terms of multi-path modeling because there is no single observable that will give just multipath. In that case, they are always faced with either combing multiple satellites or having other error sources there at the same time

(3) SNR data don't care about satellite clocks and atmospheric delays and don't need cm-level satellite orbits

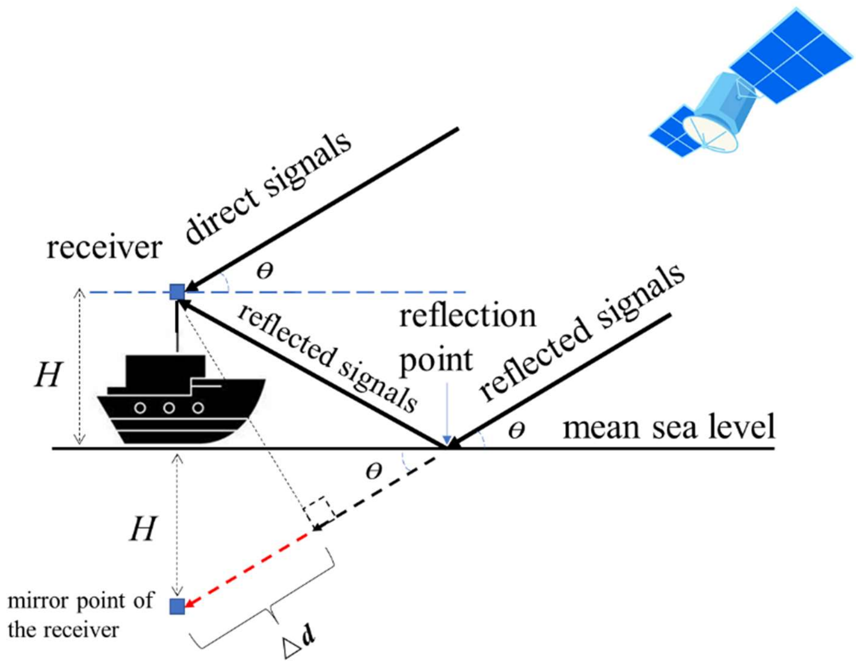

Fig.2.1 Schematic of GNSS-IR without waves

There is a direct signal that interferes with the reflected signal which travels this additional distance(△d, path length) shown in Fig.2.1 in red. so the phases of these two signals would not be the same. This phase difference depends on the distance from the mean sea surface to the antenna (H). Sometimes that direct and reflected signals are out of phase and the amplitude of the synthesized waves becomes weaker, called destructive interference. Sometimes they are in phase and the amplitude of the synthesized waves becomes stronger, called constructive interference. So the receiver records those interference patterns and that's what causes the observations. From the geometric relationship shown in Figure 2.1, the following formula can be obtained:

$$\triangle d = 2H\mathrm{Sin}(\theta) \qquad (2.1)$$

△d represents the path length, the extra distance traveled by a reflected signal; H represents the distance from the antenna to the mean sea surface; ɵ is the elevation angle.

The mixed signal can be shown as followed:

$$\text{Signal} = \underset{①}{A\cos(\Omega t)} + \underset{②}{Ar\cos(\Omega t+\varphi)} \qquad (2.2)$$

①represents the direct signal;②represents the reflected signal; Ω is the L-band frequency; φ the phase of the interference. A represents the time-dependency amplitude of the signal; r represents the ratio between the mean amplitude of direct signals and reflected signals.

According to the Trigonometric transformation, Equation (2.2) can be expressed as the following:

$$\text{Signal}=\underset{③}{\sqrt{A^2+(Ar)^2+2A^2r\cos(\varphi)}}\cos(\Omega t+\varphi) \qquad (2.3)$$

③ is the square root of the power of the signal. The expression of power of received signal is as followed:

$$\text{Power} = A^2+(Ar)^2+2A^2 r\cos(\varphi) \qquad (2.4)$$

Also from the literature[28], we know that the expression of the phase φ is as followed:

$$\varphi=\frac{4\pi H}{\lambda}\sin(\theta) \qquad (2.5)$$

λ represents the wavelength of the GNSS signal.

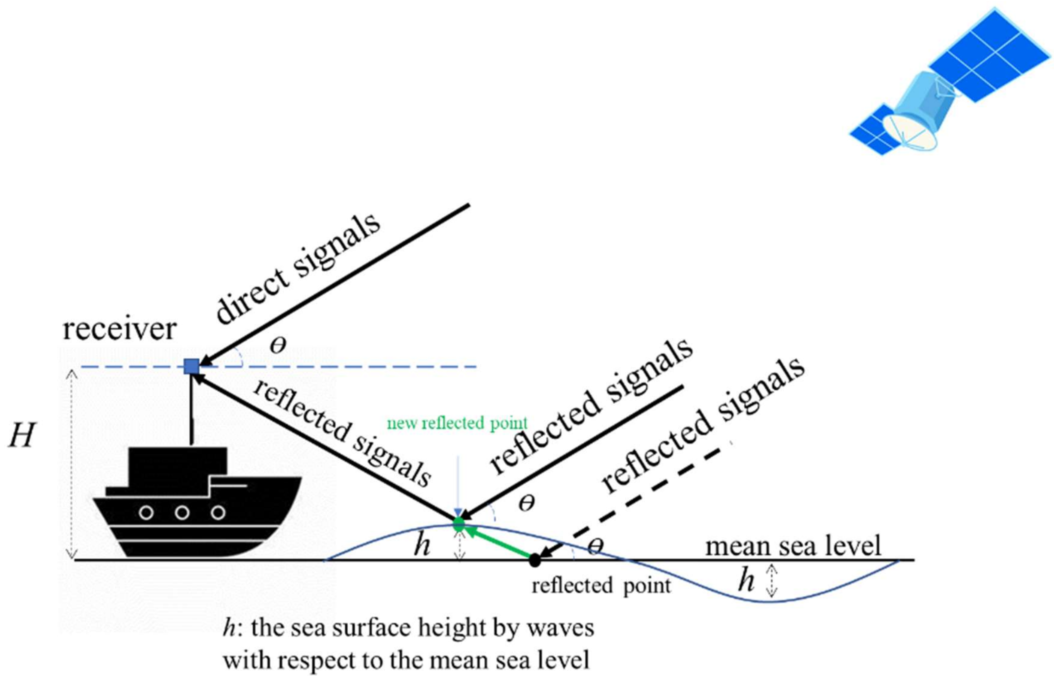

Fig.2.2 Schematic of GNSS-IR if waves exist

If a wave exists, that part of the path length (the green line in Fig.2.2) will disappear because the new reflected point (the green point in Fig.2.2) is different and higher than the old one. As known, the path delay changes will change the phase delay. If the water surface vertically moves by waves, the phase delays temporally variate, which is recognized by power changes of mixed signals (SNR, signal-to-noise ratio). In the existence of waves, the new expression for the phase and the expression is as follows:

(1) $\varphi=\frac{4\pi(H+h(t))}{\lambda}\sin(\theta)$ (2.6)

(2) $\text{Power} = A^2+(Ar)^2+2A^2 r\cos(\frac{4\pi(H+h(t))}{\lambda}\sin(\theta))$ (2.7)

2.2 The flow of the experiment

The experiment flow in Fig.2.3 will be introduced as followed.

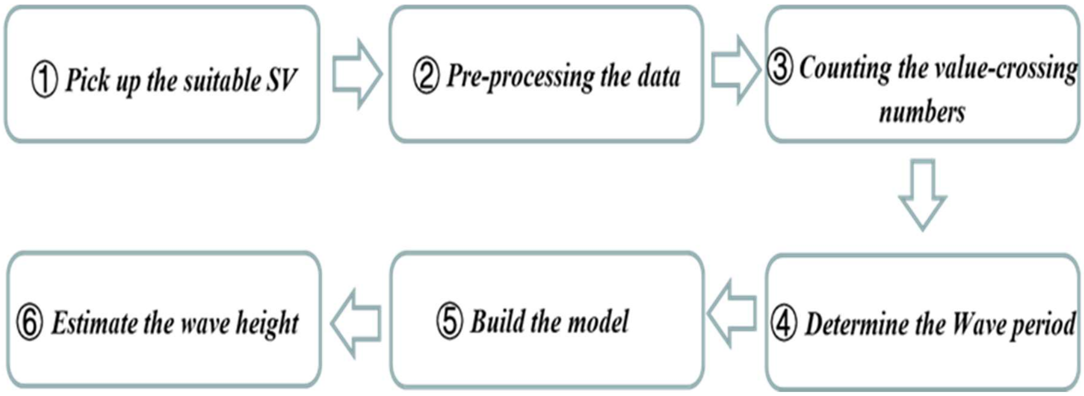

Fig.2.3 The experiment flow

2.2.1 Satellite vision and the pre-processing

Firstly, SNR data from the antenna are obtained by picking up the satellite vision with appropriate elevation and azimuth angles. Regarding the range of elevation angles, Satellite signals with low elevation angles are usually used in single antenna mode, and better results can be obtained with satellite altitude angles between 5° and 30°[29]. This is because the proportion of right-handed circular polarization (RHRP)in reflected signal is larger when the satellite elevation angle is small, and the interference effect is more positive.

Second, pre-processing measurements include removing the first few seconds of data and removing the long-term variation with the least squares method, which is a widely used method to eliminate trend terms [30]. And a few seconds after powering on, the data quality may not be good. It is necessary to remove them.

2.2.2 the Indexes of rapidness of SNR changes

For the simulation of SNR, we need to set some parameters like the distance from the antenna to the mean sea surface(H), the elevation angle of the satellite(ɵ), wave period(T), wave height(h(t)), and the ratio between the mean amplitude of direct signals and reflected signals(r). The h(t), the sea surface change by a single wave with time series, is shown in Fig.2.4.

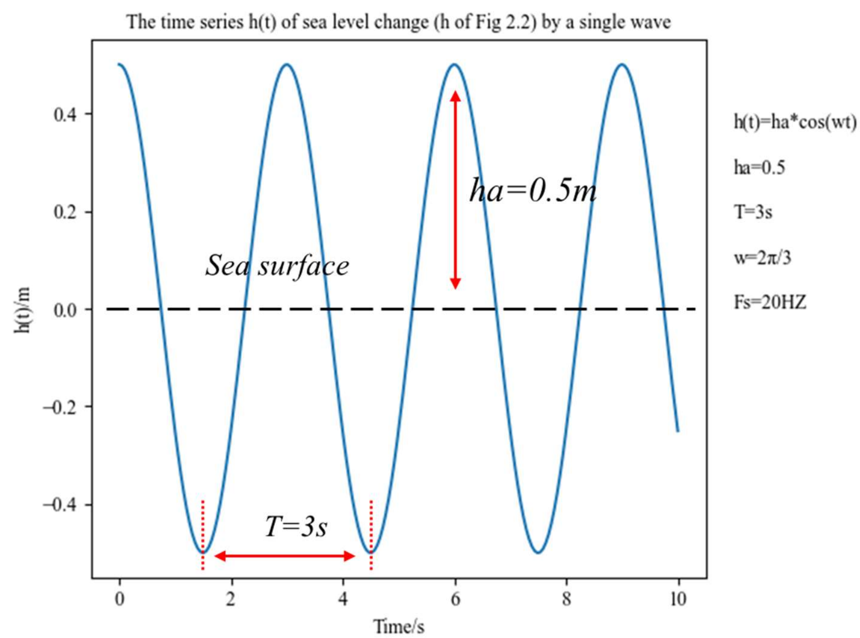

Fig.2.4 The time series h(t) of sea level height change (h of Fig2.2) by a single wave

h(t) is assumed as 0.5*cos(wt) from the Fig.2.4. The simple SNR curve by Equation (2.7) is shown in Fig.2.5. The SNR curve includes many high-frequency variations.

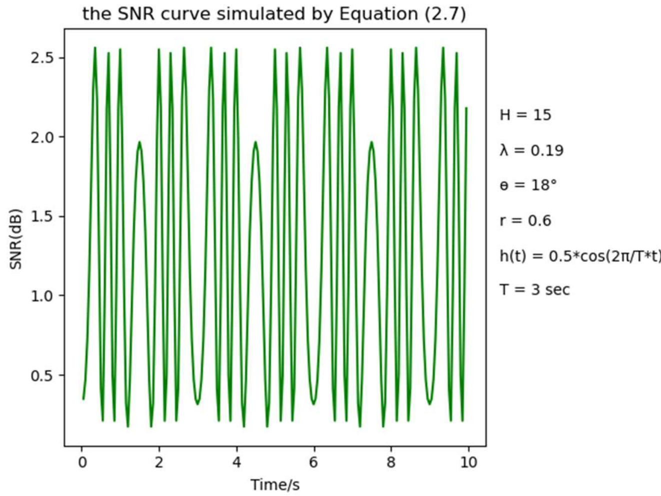

Fig.2.5 simple SNR curve simulated by Equation (2.7)

It is known that the SNR curve includes lots of high-frequency variations, since every time when the phase delay becomes zero, SNR becomes local maximum. Therefore, the number of these high-frequency variations would correspond to the number of interference stripes with every 0.19m (L1 band wavelength of GNSS signals, λ). In Fig.2.6, many red lines intersect the SNR curve and the number crossing are marked in red. In this study, we use the method of counting the number crossing (red points in Fig.2.6) for high-frequency variations.

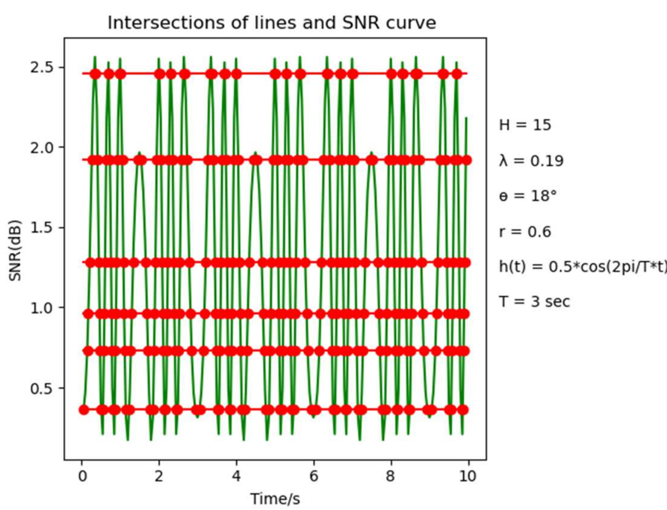

Fig.2.6 intersections of lines and SNR curve

Because we don't know initial phase and avoid it's dependency, it is necessary to set 100 lines between the maximum and minimum of SNR and counting the number crossing of each line with SNR and after trying different threshold, we select the average value or 50th as the threshold. In Fig.2.7, the relationships of threshold and number crossing with different SWH based on single-wave model are shown. Obviously, the maximum and minimum in threshold is not suitable and the thresholds in the range A from 25 to 75 are better.

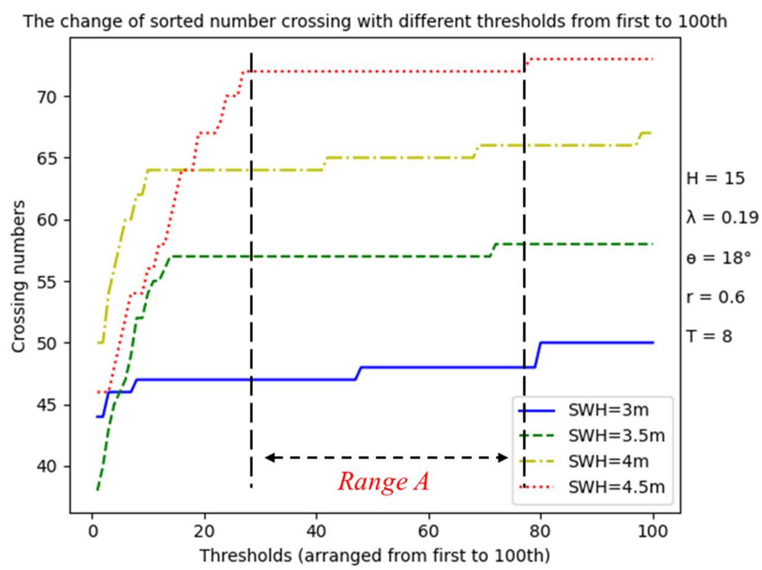

Fig.2.7 The relationship of thresholds and number crossing with different SWH

2.2.3 the wave period estimation

Because we have known that the pattern of SNR is repeated with every wave period(3s) in Fig2.6, we can use ACF (Autocorrelation Function) to determine the wave period. Before determining the wave period, the “half envelope” of the data should be extracted, which is connected by the local maximum and could reduce the influence of factors such as high-frequency noise on the ACF. For example, the “half envelope” is in orange in Fig.2.8. Then, use ACF to determine the wave period. The result of ACF from the example is shown in Fig.2.9 and Horizontal coordinate of the first peak is around 60 lags close to the wave period 3s we set. From that, we can normalize the numbers.

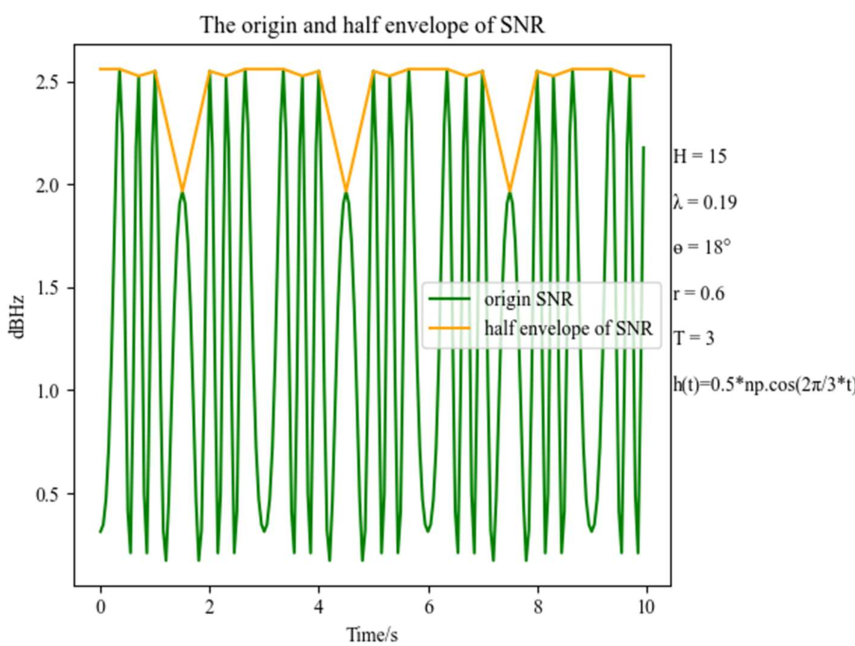

Fig.2.8 The origin and half envelope of SNR

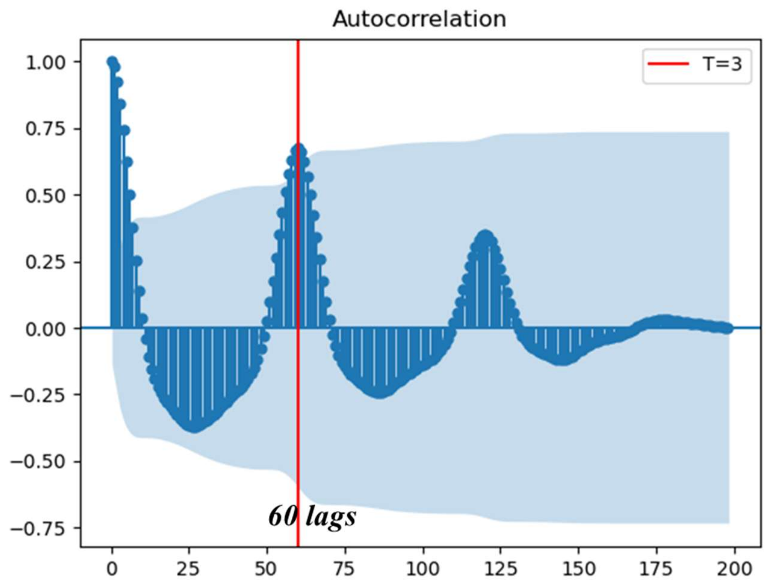

Fig.2.9 The result of ACF

2.2.5 Build the model and SWH estimation

Lastly, according to the relationship between the number of high-frequency variations and the number of interference stripes. we build the models between the numbers crossing and SWH. Different types of models will be introduced in the later chapter. With the help of models, a significant wave height can be estimated.

CHAPTER 3: Result

3.1 wave simulation

3.1.1 Single-frequency wave simulation

It is assumed that the wave of single frequency exists. h(t) in equation 2.7 can set the amplitude of the wave (ha) times the cos wave at some angular frequency. As we know, A is the time-dependency amplitude of the signal. If the observation time is only a few minutes, that A doesn't change much and it can be treated as a constant. So equation 2.7 can be simplified as followed:

$$Power = 1+r^2+2r\cos(4\pi(H+ha*\cos(2\pi/T t))/\lambda \sin(\theta)) \quad (3.1)$$

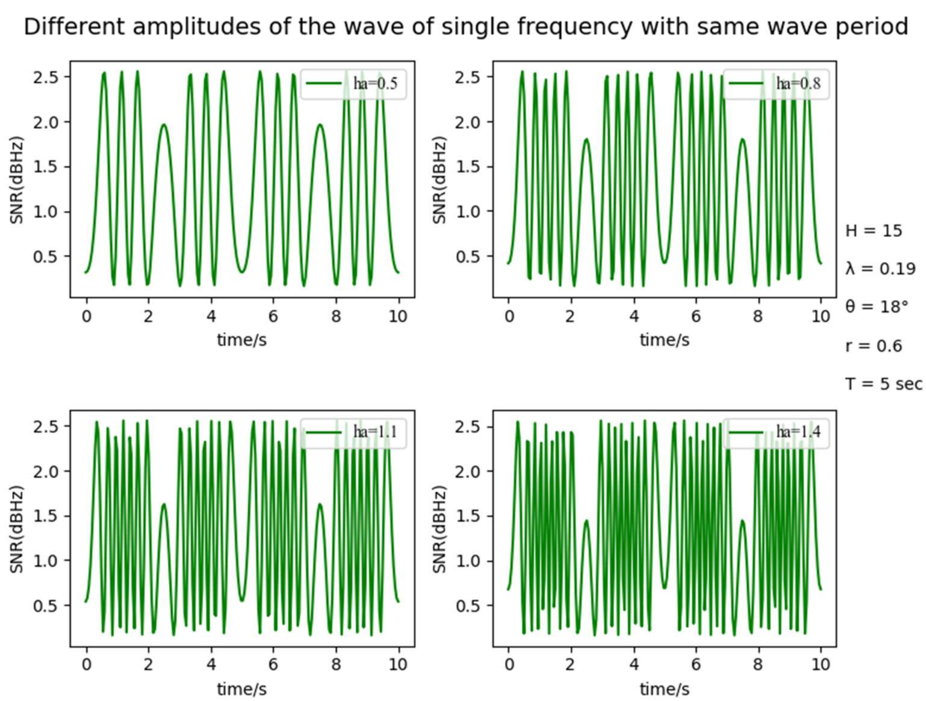

Fig.3.1 Different amplitude of the wave of single frequency with the same wave period

From Fig.3.1, one of the SNR patterns is that there are more and more high-frequency variations with the amplitude of the wave of single frequency increases.

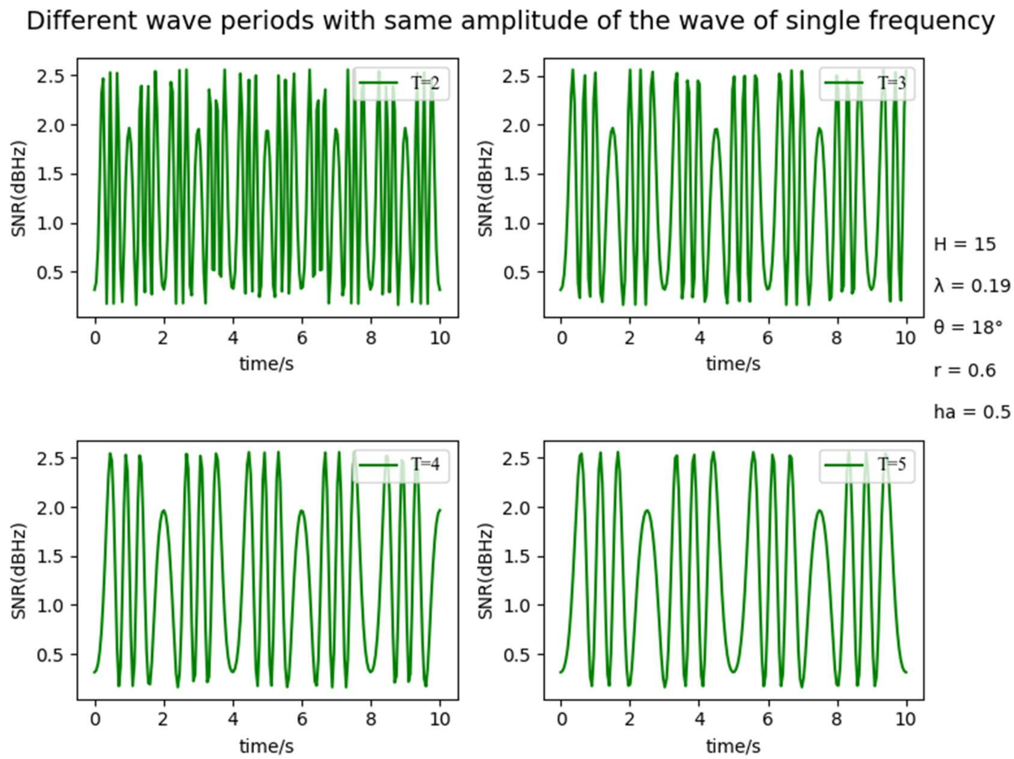

Fig.3.2 Different wave periods with the same amplitude of the wave of single frequency

From Fig.3.2, another pattern of the SNR patterns is that a similar pattern will occur every wave period. Those patterns show that the time series of SNR is periodic and the change of the sea surface by waves at the observation point feeds back well in the image of SNR. The model of the number crossing and the significant wave height can be established. In Fig.3.3, that relationship is shown with three curves of different wave periods.

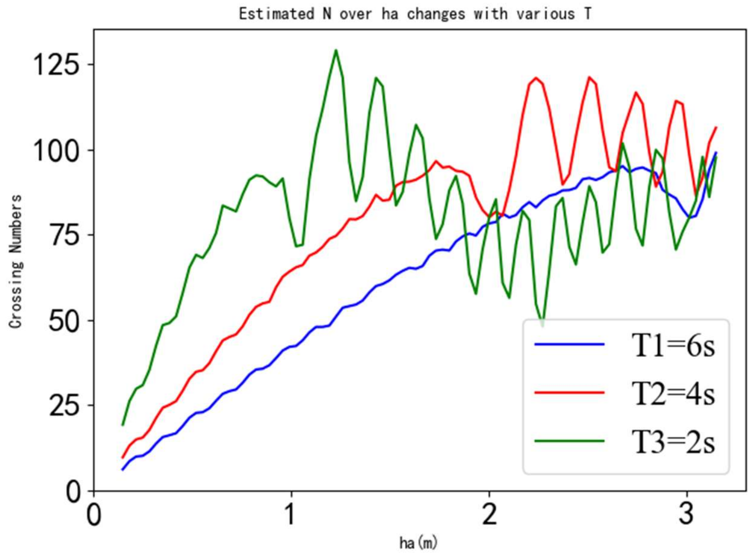

Fig.3.3 Estimated N over ha changes with various T

In Fig.3.4, the ratios of crossing numbers among those three different wave periods are demonstrated. The results are compared to the line of fixed value (4/6,2/4) and they are almost the same. It is only related to the period when other parameters are fixed, so it can be normalized.

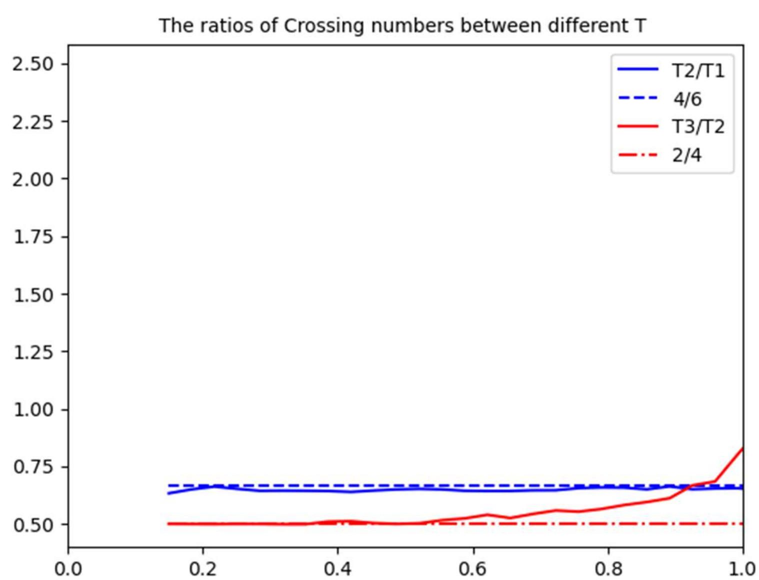

Fig.3.4 The ratios of Crossing numbers between different T

After normalization, the model of the crossing number and the significant wave height that should be twice the amplitude of the single wave (2*ha) is shown in Fig.3.5. The estimated crossing number shows the near-linear increase with the significant wave height for various T. However, no significant increase in number crossing is recognized when 2*ha exceeds around 1.5m,3.5m, and 5.5m respectively. It shows only periodic fluctuations with time series. This is the limitation of sampling frequency.

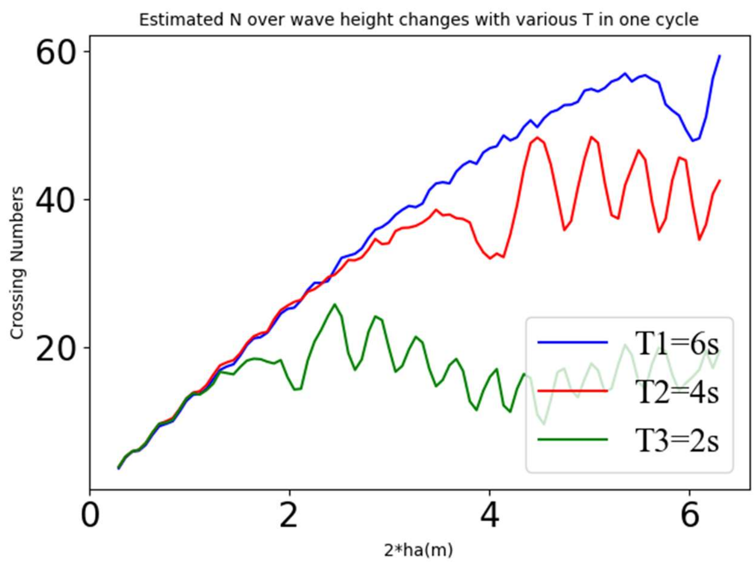

Fig.3.5 Estimated N over wave height changes with various T in one cycle

3.1.2 Dependency of the ratio(r) the distance (H)

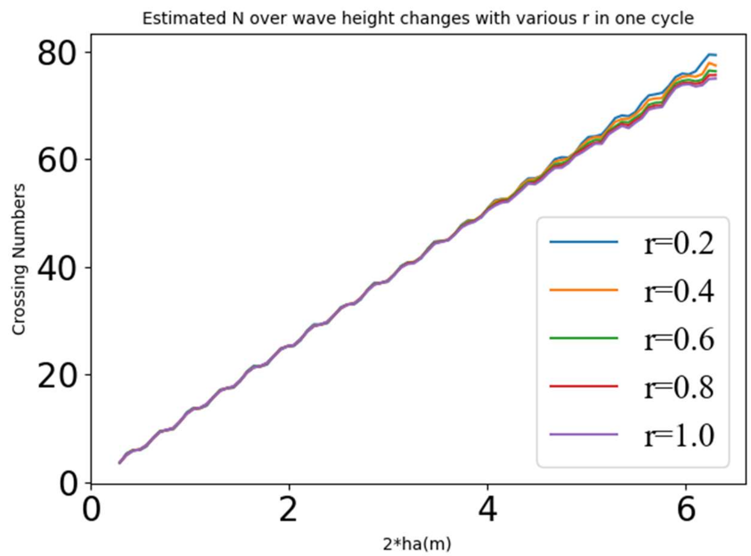

Fig.3.6 Estimated N over wave height changes with various r in one cycle

In.Fig.3.6, there are only little differences among various r. In normal conditions, the change of the r of parameters has little influence on the result of number crossing.

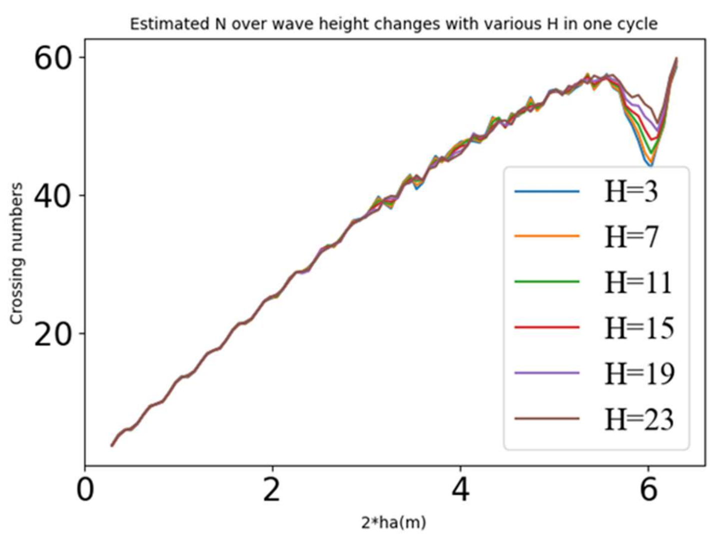

Fig.3.7 Estimated N over wave height changes with various H in one cycle

In Fig.3.7, It is shown that there is no significant change with different H because the change of H doesn't affect the speed of phase change from Equation 2.6. We estimate the numbers crossing as the average of the number of intersection points where 100 different lines intersect the SNR curve.

3.1.3 Dependency of the elevation angles (ɵ) and wavelength of GNSS (λ)

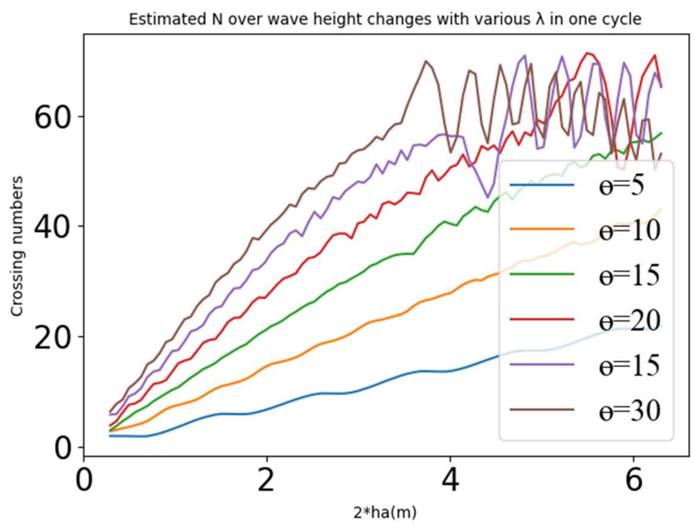

Fig.3.8 Estimated N over wave height changes with various r in one cycle

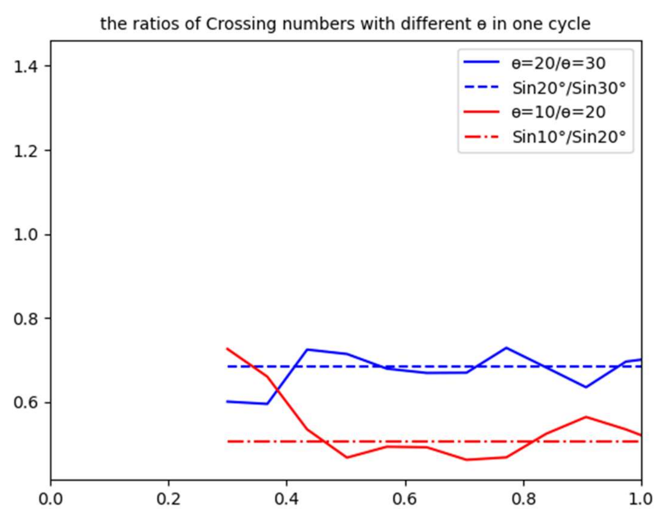

Fig.3.9 the ratios of Crossing numbers with different ɵ in one cycle

From fig.3.8, it is learned that number crossing become more with the elevation angle increase. That is because sin(ɵ) becomes larger as the ɵ increases and ha also becomes larger when a change of the path delay is fixed, which needs more number crossing. In Fig.3.9 the results are compared to the line of fixed value (Sin20°/Sin30°, Sin10°/Sin20°) and they are almost the same. It is only related to the sin(ɵ) when other parameters are fixed.

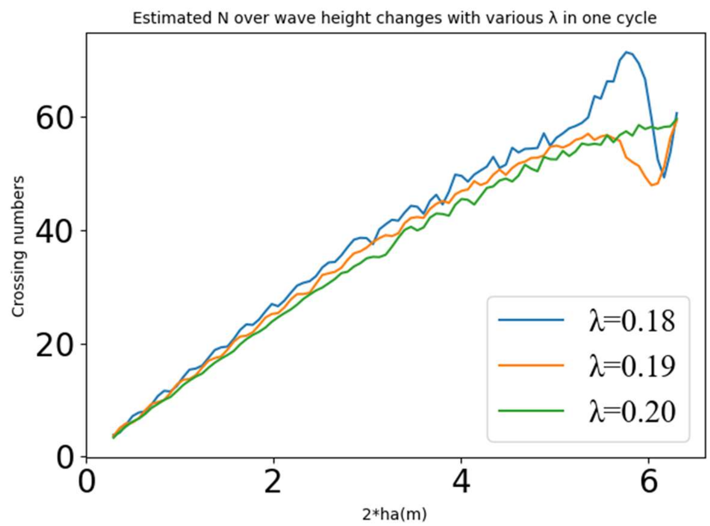

Fig.3.10 the ratios of Crossing numbers with different ɵ in one cycle

From Fig.3.10, there are a few differences among the different wavelengths. As known, different satellite systems have their L-band wavelength, for example, the L1-band wavelength of GPS is around 0.19m(frequency:1575.42x10^6Hz). It makes a little different change when the phase becomes zero every time because of the constructive interference with different wavelengths.

3.1.4 Multi-frequency wave simulation with ISSC Spectrum

Instead of single-frequency wave, almost the waves are combined in practice. In this study, the model of the ISSC Spectrum is used for the simulation. The ISSC spectrum (also known as

Bretschneider or modified Pierson-Moskowitz) is defined as

$$S(f)=\frac{5}{16}Hs^2 f_m^4 f^{-5} \exp[-\frac{5}{4}(\frac{f}{fm})^{-4}]$$

Where f is frequency. The other two parameters, the peak frequency fm and the significant wave height Hs, are data items[31]. It is known that the ISSC spectrum gives amplitudes information and no phase information, and the phase can be provided at random. For each frequency, the amplitude and phase could be obtained. Then, use the inverse of Fast Fourier Transform (IFFT) to convert it into time series. Because the SWH of the sea level time series would depend on phases of the spectrum, we cannot determine exact SWH values from the spectrum directly, unless there is an infinite length of data recorded. The actual SWH can be extracted from the time series with the definition of significant wave height. The next step is to replace the h(t) in Equation 2.7 with that the list of actual SWH.

In Fig.3.11, the curve of the ISSC Spectrum is demonstrated. The peak frequency is 0.2Hz and the spectrum has already included the combined waves with many different frequencies.

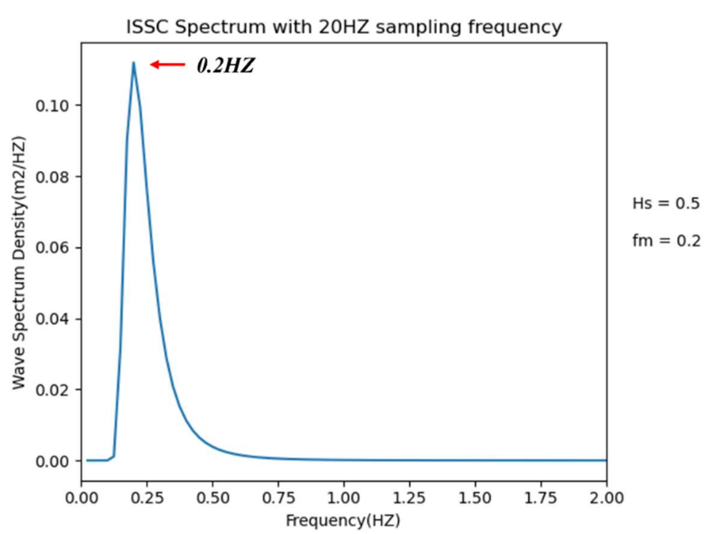

Fig.3.11 The ISSC Spectrum with 20Hz sampling frequency

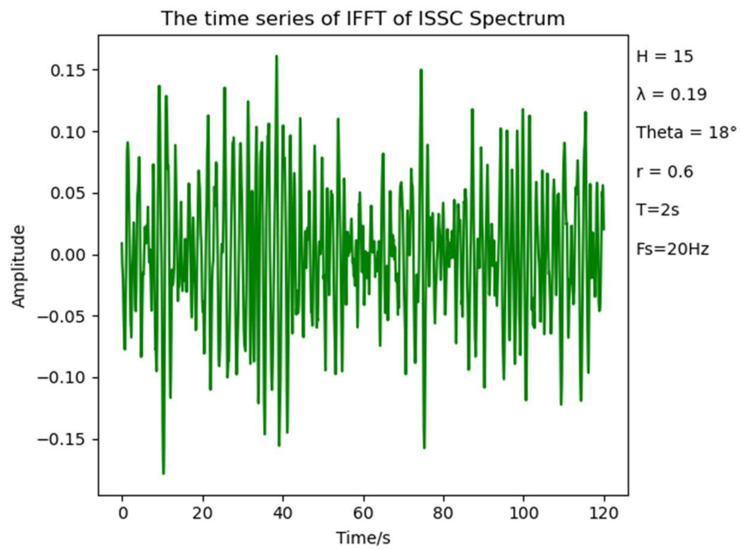

Fig.3.12 The time series of IFFT of ISSC Spectrum

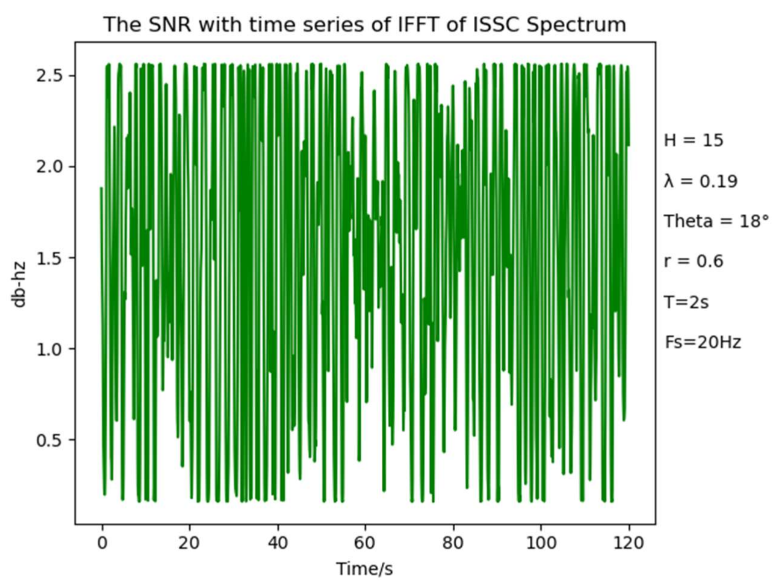

Fig.3.13 The SNR with time series of IFFT of ISSC Spectrum

The result of example in Fig.3.12 after converting the ISSC Spectrum into time series is different from that of single frequency in Fig.2.4. Based on the Equation (2.7), the SNR curve can be obtained in Fig.3.13.

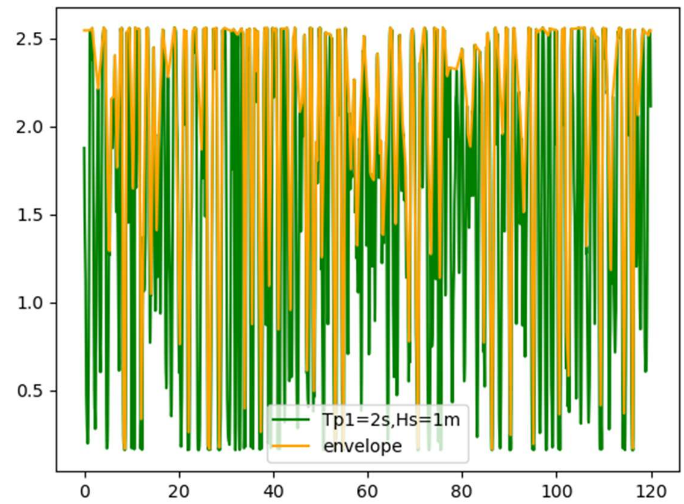

Fig.3.14 The origin and half envelope of SNR

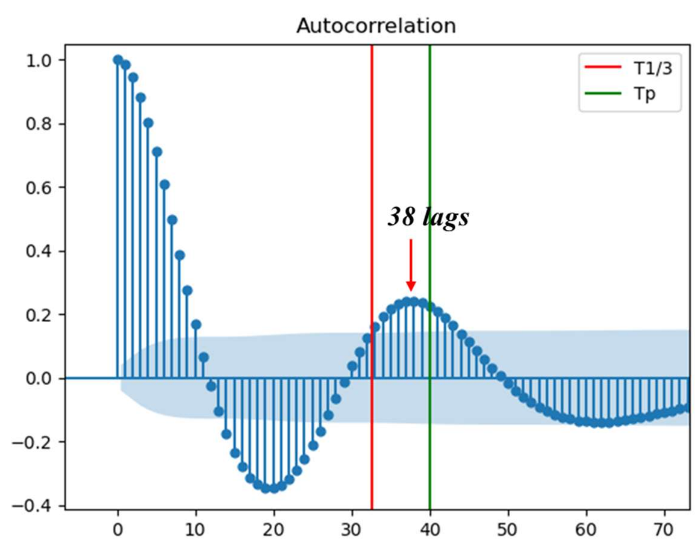

Fig.3.15 The result of ACF

Based on the example of Fig.3.13, the “half envelope” is in orange in Fig.3.14. The result of ACF from example is shown in Fig.3.15 and the horizontal coordinate of the first peak in ACF is around 38 lags (1.9s) closed to the significant wave period(red) and peak wave period(green) 2s as the text of Fig.3.13 shown.

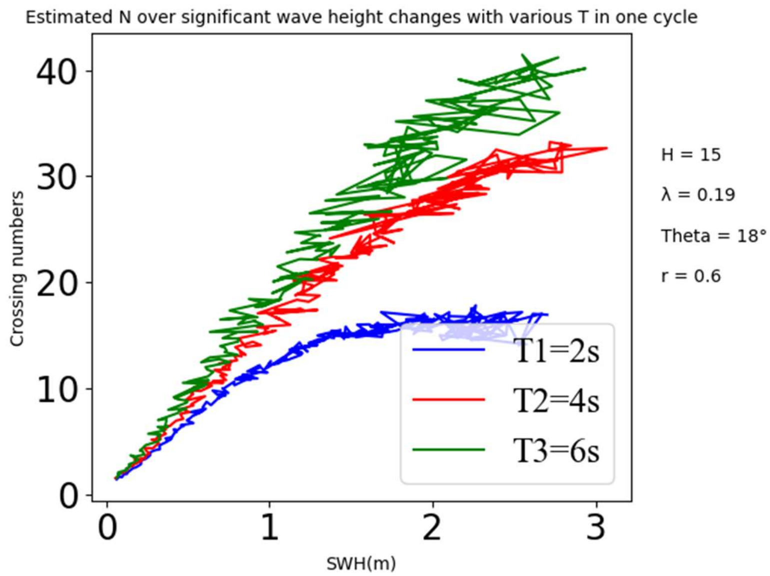

Fig.3.16 Estimated N over significant height changes with various T in one cycle

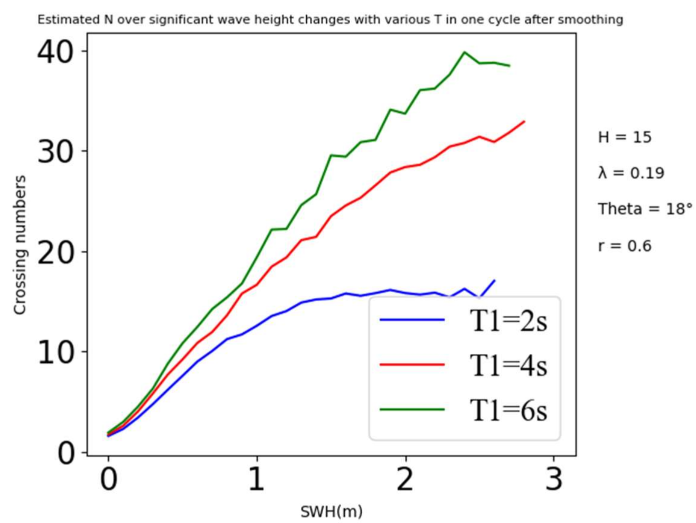

Fig.3.17 Estimated N over significant height changes with various T in one cycle after convolution

The relationship between numbers crossing and significant wave height is shown in Fig.3.16. Because of the random phase, even with the same SWH, their crossing numbers might be different. In order to estimate the SWH better with actual data, smoothing is used in Fig.3.17.

3.2 Validation

3.2.1 Observation area and SNR data on shipborne

The observation area is situated in Tsushima strait and the antenna is on the right-front side of ship, “*New Camelia*”. Fig.3.18, it is shown the sailing route of “New Camelia” across Tsushima Strait and runs between Hakata Port and Busan Port. The calendar is also demonstrated from Jan 2005.

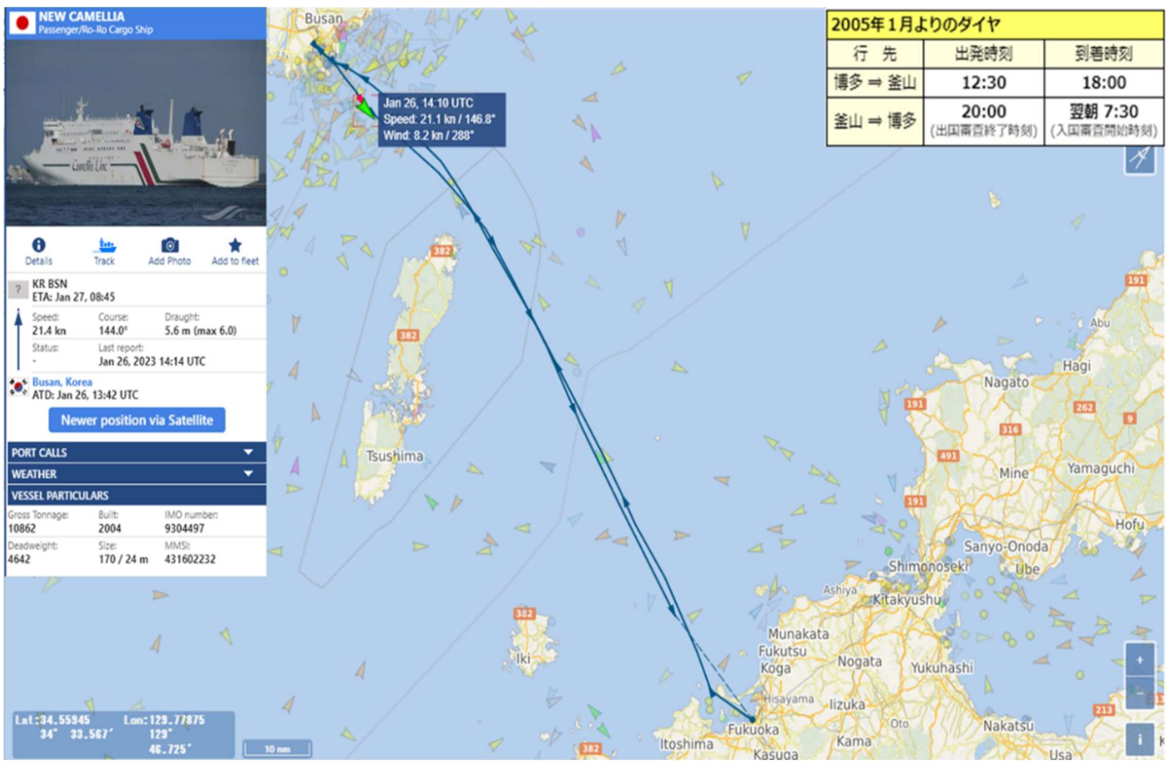

Fig.3.18 The sailing route in blue and the position of “*New Camelia*” at Jan 26, 2023 14:14 UTC

(Retrieved from: https://www.vesselfinder.com/?imo=9304497)

As for SNR data received by the single antenna, the sampling frequency is 20Hz and the data duration is 2 minutes with hourly observation. The example of actual SNR data is shown in Fig.3.19

and there are much more noises than that of simulated data in Fig.2.5. Thus, it is necessary to take the measurements of extracting the "half envelope" to determine the wave period accurately. Also, the long-term variation in the red dashed line is not removed. In fact, the actual data is not continuous and there are some small gaps in the time series to be addressed.

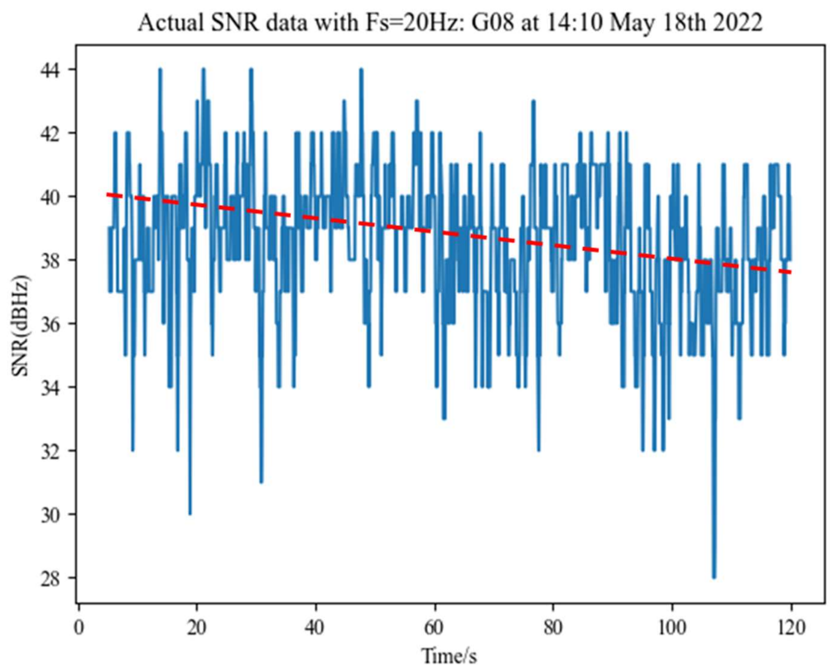

Fig.3.19 Actual SNR data with Fs=20Hz: G08 at 14:10 May 18th 2022

For example, of actual SNR data: G08 at 14:10 May 18th 2022, the "half envelope" is in orange in Fig.3.20. The result of ACF from example is shown in Fig.3.21 and horizontal coordinate of the first peak in ACF is 76 lags (3.8s) closed to the actual wave period 3.6s from the calibration data system (*Polaris Hindcast*).

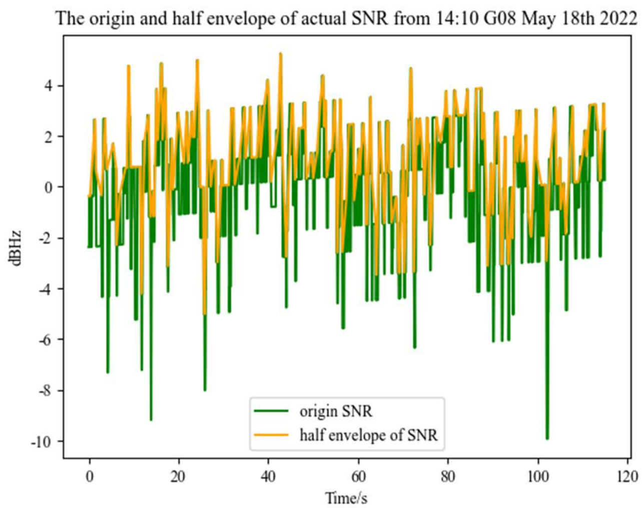

Fig.3.20 The origin and half envelope of actual SNR from 14:10 G08 May 18th 2022

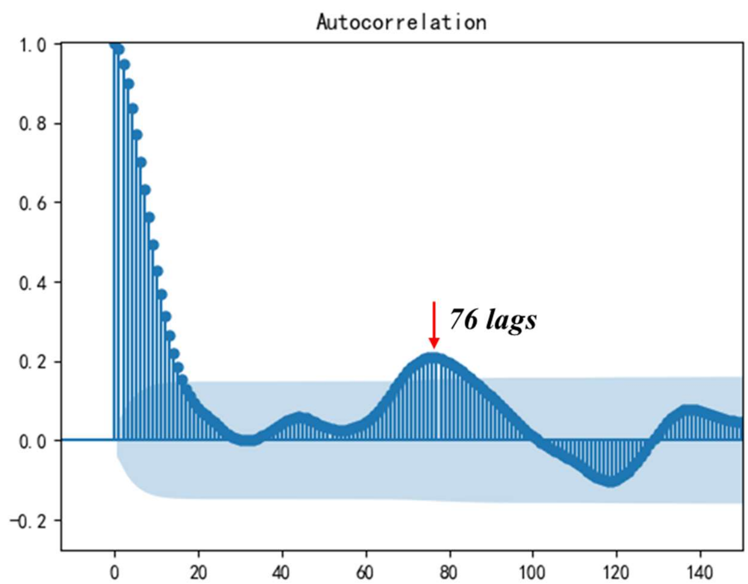

Fig.3.21 The result of ACF

we choose three cases in different sea states, which are in calm sea state, standard sea state, and rougher sea state respectively. The results of significant wave heights can be estimated from the single-frequency wave model and multi-frequency wave model of ISSC Spectrum. Then, the obtained results are compared to the actual data from the calibration data system (*Polaris Hindcast*). The patterns could be found in different sea states with the same model and in different models with the same sea state.

3.2.2 Calm sea state

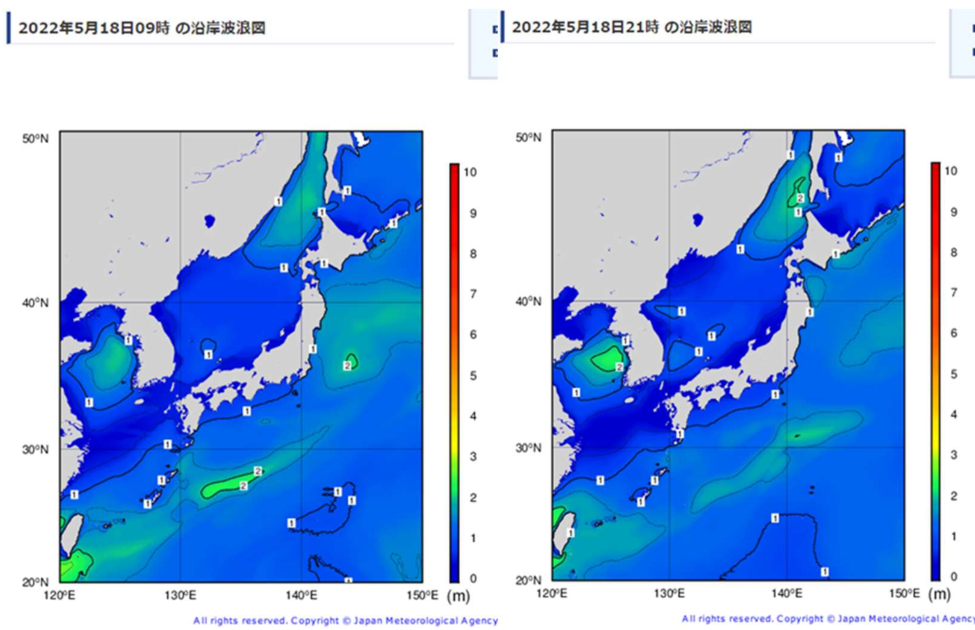

Fig.3.22 Coastal Waves in Japan and Nearby Regions at 9 am and 21 pm on May 18th, 2022(Note: Japan Meteorological Agency report; Retrieved from: https://www.data.jma.go.jp/gmd/kaiyou/db/wave/chart/daily/coastwave.html)

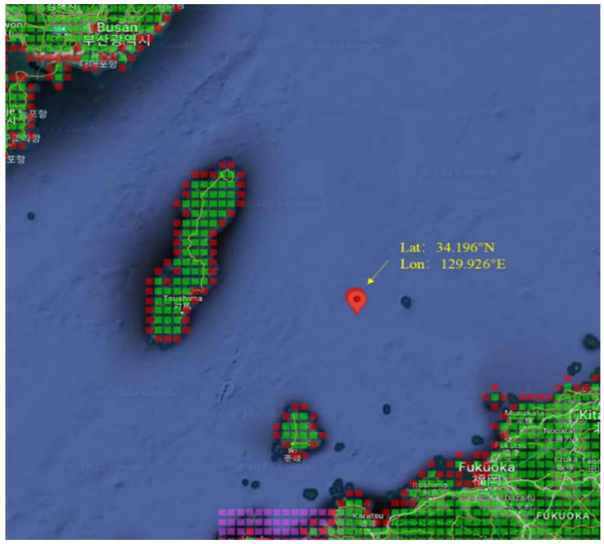

Fig.3.23 the position of “New Camelia” at 14:10 May 18th 2022(Retrieved from:

https://polaris.jwa.or.jp/hindcast/hindcastinput)

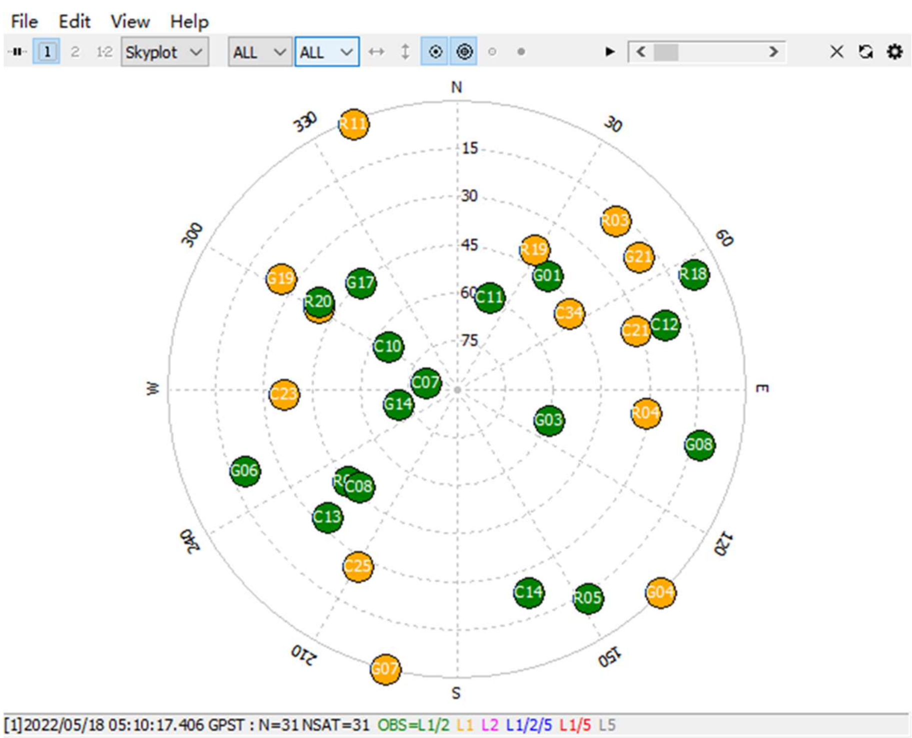

Fig.3.24 the sky plot of the Satellites vision at 14:10(UTC) on May 18th, 2022

From Fig.3.22(JMA report), the sea state on May 18th, 2022 is calm, and the significant wave heights are less than 1m. The SNR data we used is at 14:00(UTC) on that day. the ship is marked in red point in Fig.3.23. From Fig.3.24 of the sky plot, the potions of kinds of satellites are shown at 14:00(UTC) on May 18th, 2022. Based on the latitude and longitude of the observation area, the position of the antenna on the ship, and the range of elevation angles, we choose the G08 and C21 as the data sources. The bar of the result and actual data is as followed.

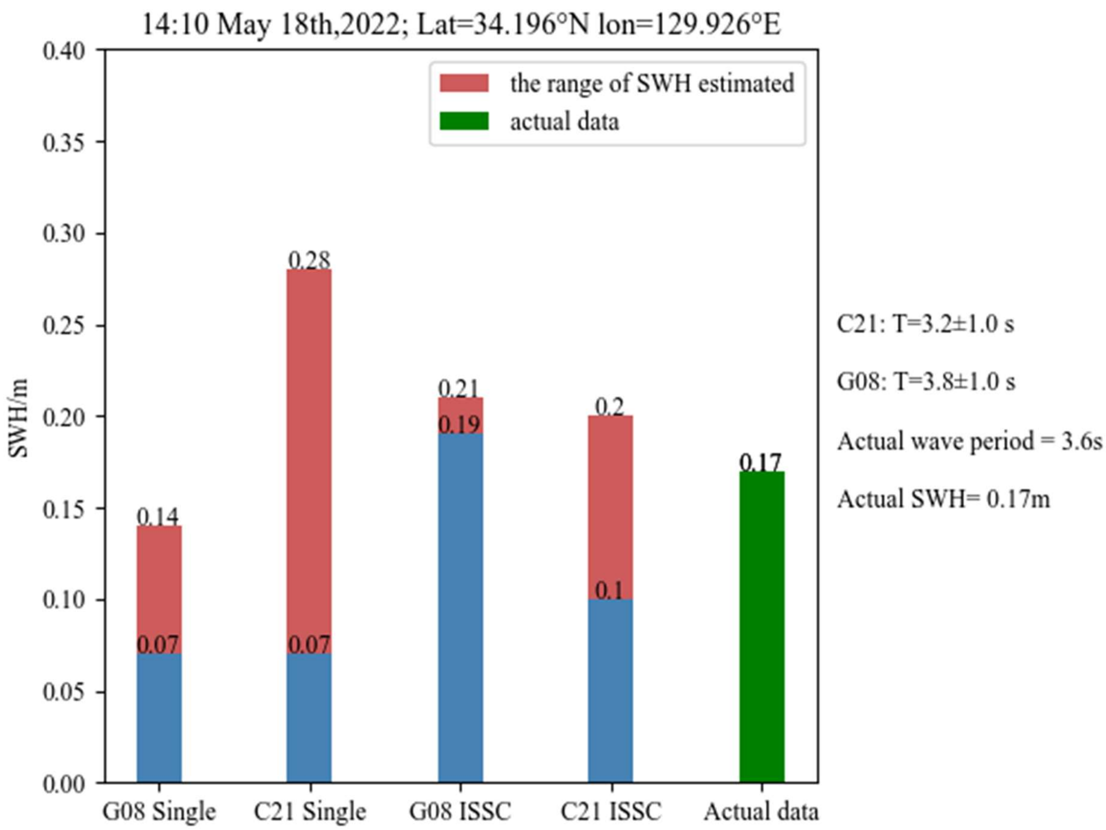

Fig.3.25 the result of SWH with different simulation models at 14:10(UTC) May 18th 2022

The wind direction is 246.6°. The estimation of wave period of G08 and C21 are expressed as the range shown in Fig.3.25. So the results of them are also expressed as the range and are close to the actual SWH, and the same satellite visions are also close to each other in different models.

3.2.3 Standard sea state

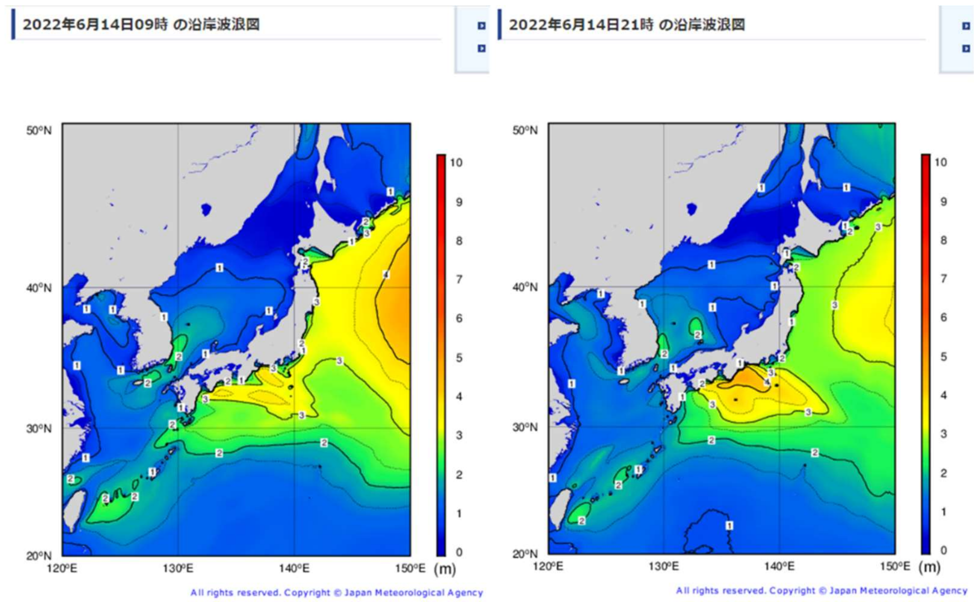

Fig.3.26 Coastal Waves in Japan and Nearby Regions at 9 am and 21 pm on Jun 14th, 2022(Note: Japan Meteorological Agency report; Retrieved from: https://www.data.jma.go.jp/gmd/kaiyou/db/wave/chart/daily/coastwave.html)

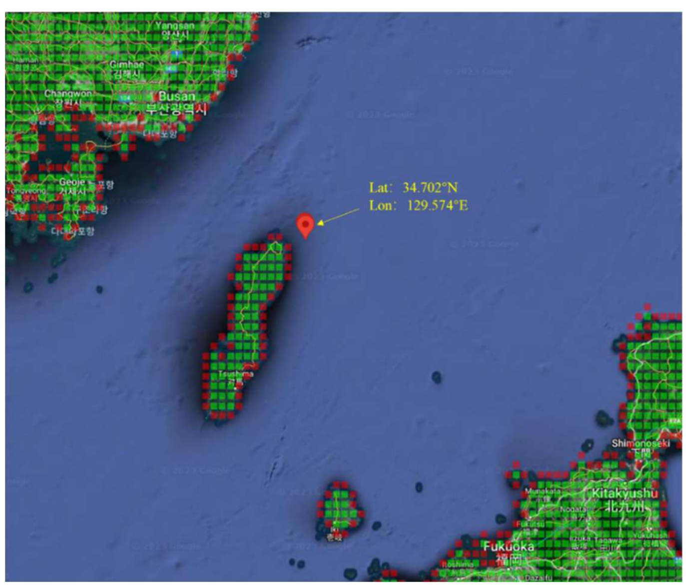

Fig.3.27 the position of "New Camelia" at 16:10 Jun 14th 2022(Retrieved from: https://polaris.jwa.or.jp/hindcast/hindcastinput)

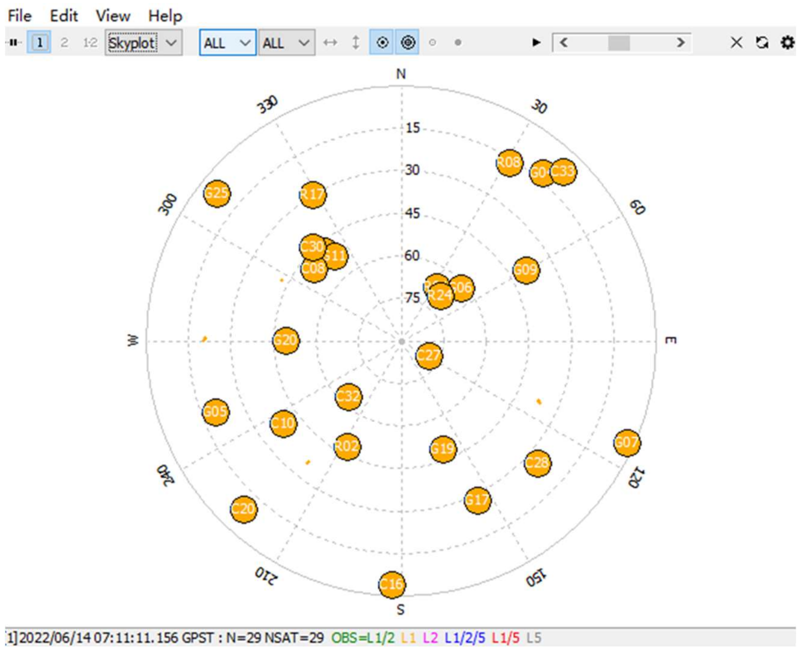

Fig.3.28 the sky plot of the Satellites vision at 16:10(UTC) on Jun 14th, 2022

From Fig.3.26(JMA report), the sea state on Jun 14th, 2022 is standard, and the significant wave heights are around 1.5m. The SNR data we used is at 16:10(UTC) on that day. At that time, the ship marked in red point is sailing around the Tsushima Island in Fig.3.27. From Fig.3.28 of the sky plot, the potions of kinds of satellites are shown at 16:10(UTC) on June 14th, 2022. Based on the latitude and longitude of the observation area, the position of the antenna on the ship, and the range of elevation angles, we choose the G04 and C33 as the data sources. The bar of the result and actual data is as followed.

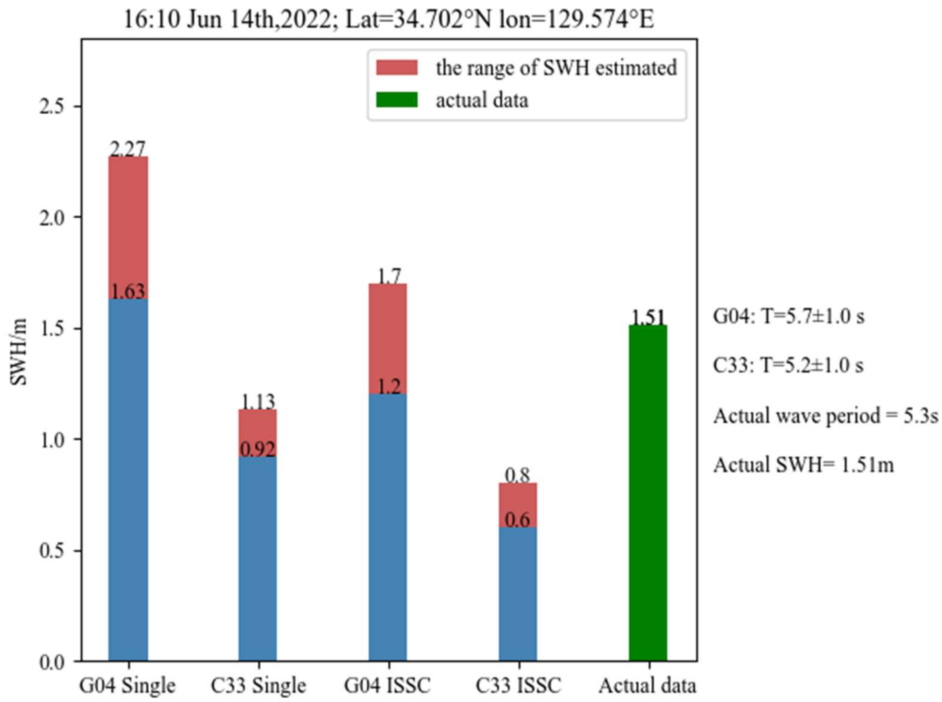

Fig.3.29 The result of SWH with different simulation models at 16:10(UTC) Jun 14th 2022

Although the solution of wave height in Weather Forecast is 0.5m, there are still differences from the actual SWH in Fig.3.29. The wind direction is 84°(almost from east to west). It can be explained that the ship is close to Tsushima Island and the SWH becomes smaller because of the impacts of the island coast.

3.2.4 Rougher sea state

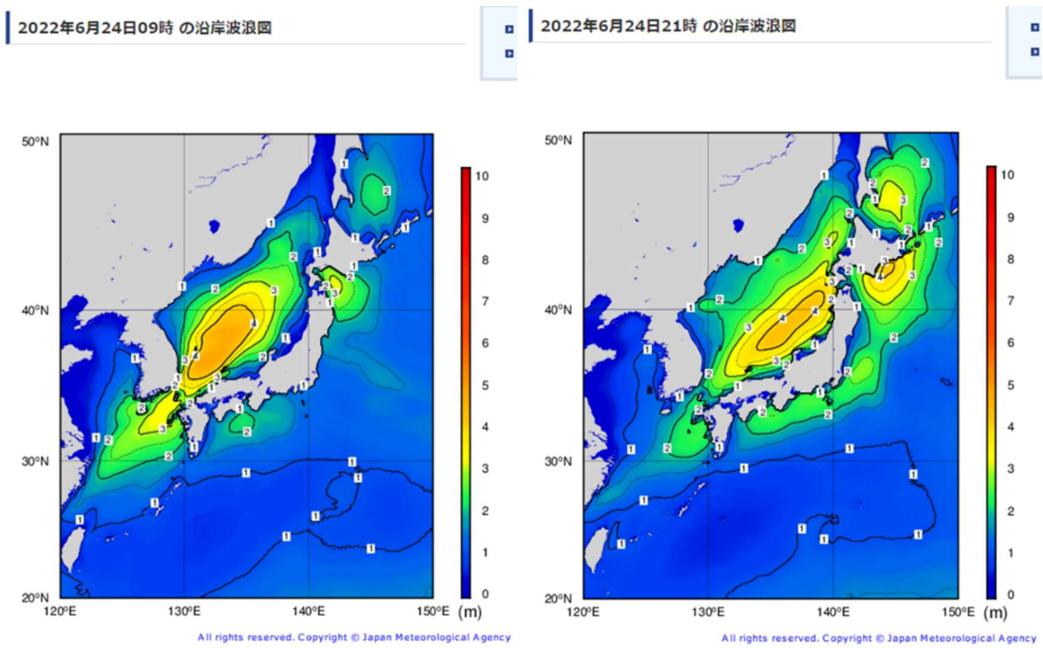

Fig.3.30 Coastal Waves in Japan and Nearby Regions at 9 am and 21 pm on Jun 24th, 2022(Note: Japan Meteorological Agency report; Retrieved from: https://www.data.jma.go.jp/gmd/kaiyou/db/wave/chart/daily/coastwave.html)

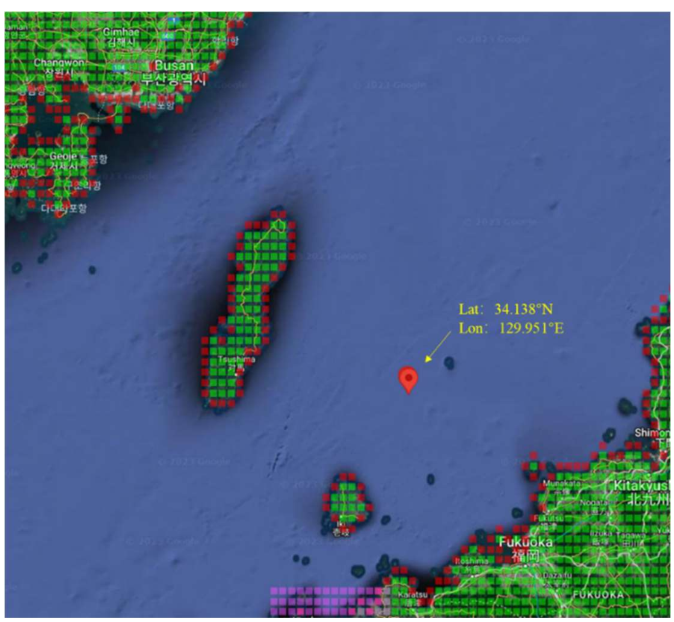

Fig.3.31 The position of "New Camelia" at 14:10 Jun 24th 2022(Retrieved from:

https://polaris.jwa.or.jp/hindcast/hindcastinput)

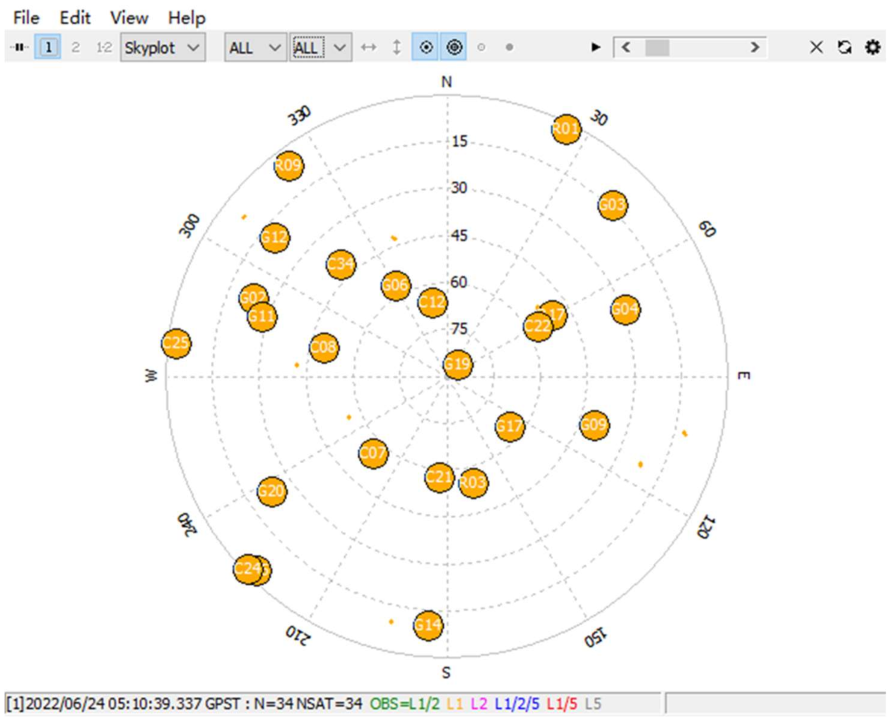

Fig.3.32 The sky plot of the Satellites vision at 14:00(UTC) on Jun 24th, 2022

From Fig.3.30(JMA report), the sea state on Jun 24th, 2022 is rougher, and the significant wave heights are more than 2m. The SNR data we used is at 14:10(UTC) on that day. At that time, the ship is marked in red point in Fig.3.31. From Fig.3.32 of the sky plot, the potions of kinds of satellites are shown at 14:10(UTC) on June 24th, 2022. Based on the latitude and longitude of the observation area, the position of the antenna on the ship, and the range of elevation angles, we choose the G03 and R24 as the data sources. The bar of the result and actual data is as followed.

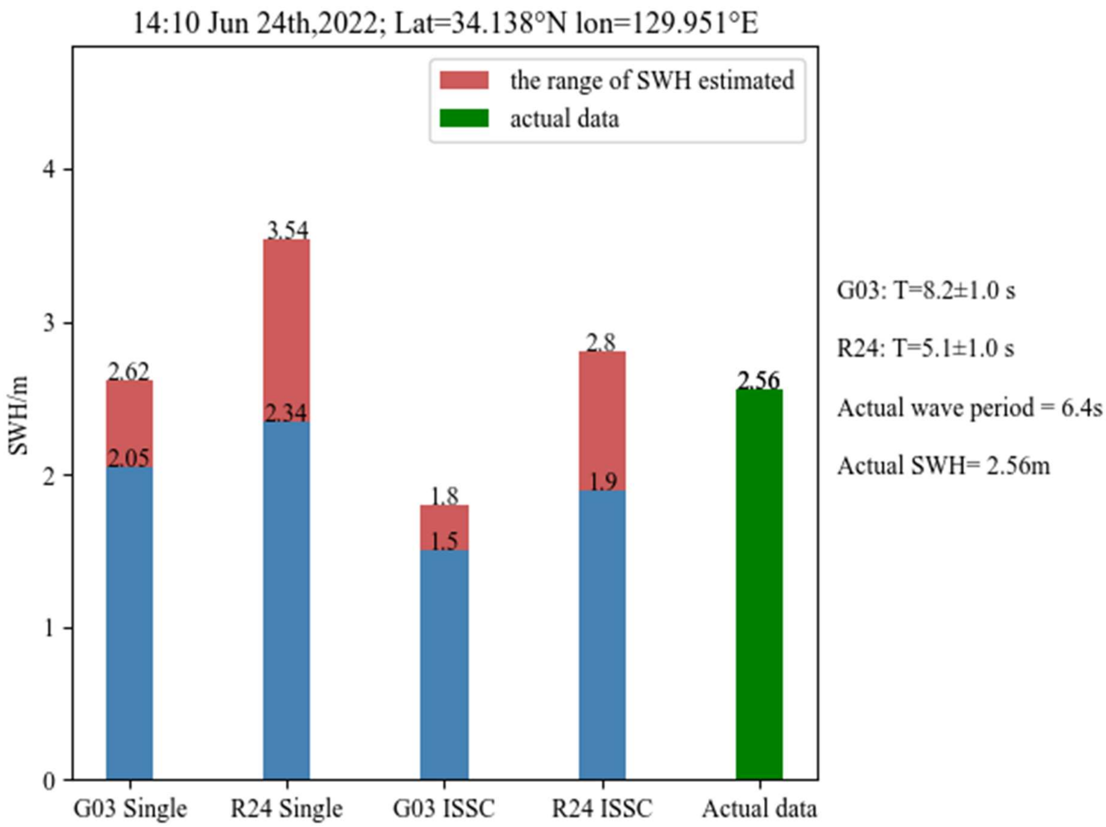

Fig.3.33 The results of SWH with different simulation models at 16:10(UTC) Jun 14th 2022

The wind direction is 212.8°. In Fig.3.33, There are huge different between the results from the single-frequency wave models and multi-frequency waves models of ISSC Spectrum at the same satellite vision. That is because the differences in crossing numbers become larger as SWH increases by comparing the Fig.3.5 to Fig.3.17. Differences in models lead to differences in results.

3.2.5 Intercomparison of results

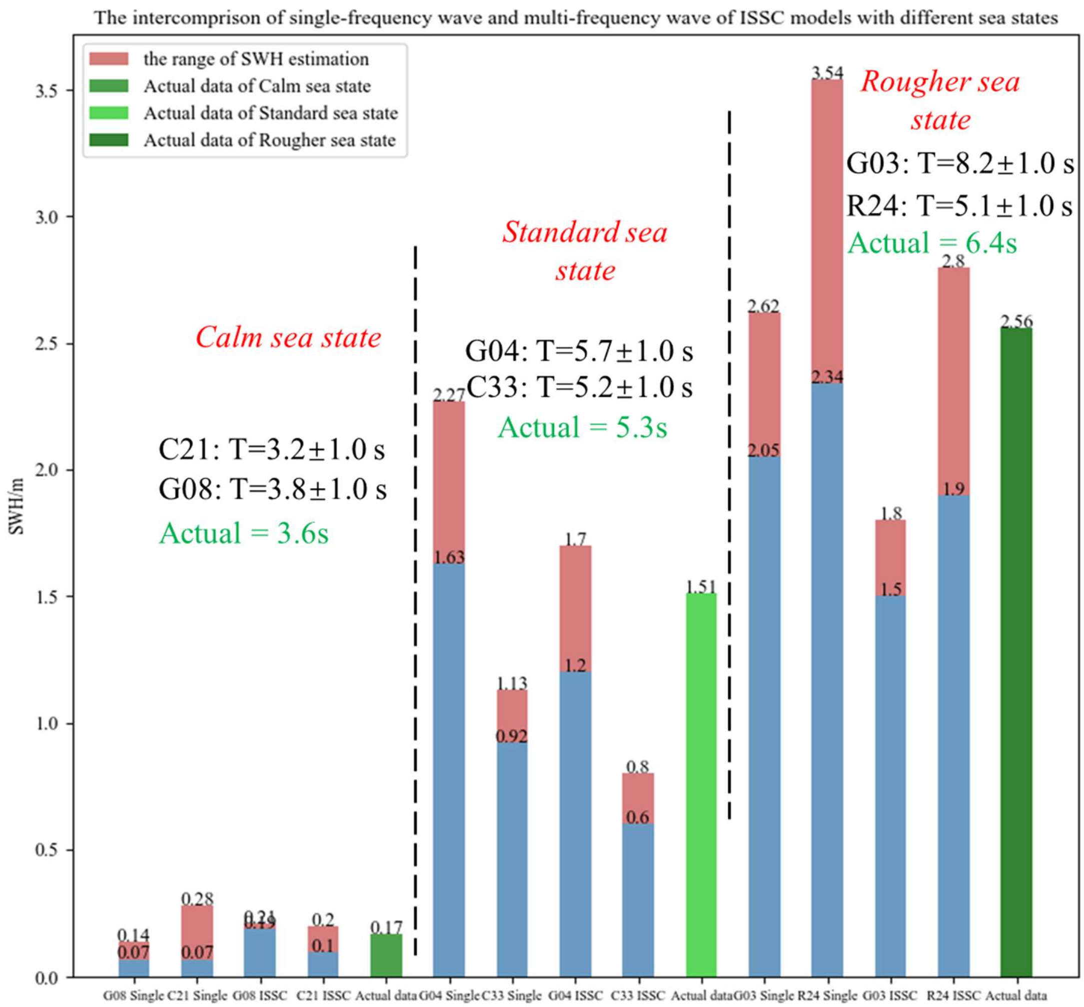

Fig.3.34 The intercomparison of single-frequency and multi-frequency wave model of ISSC Spectrum with different states

For better comparison, Fig.3.34 is combined of Fig.3.25, Fig.3.29 and Fig.3.33. In Fig.3.34, it is shown that the SWH estimated increases with the different sea states in both models. In other words, the SWH estimated increases with the sea state becoming more intense. But we can notice that the result of the wave period estimation is not so good and that is because of the duration of the data.

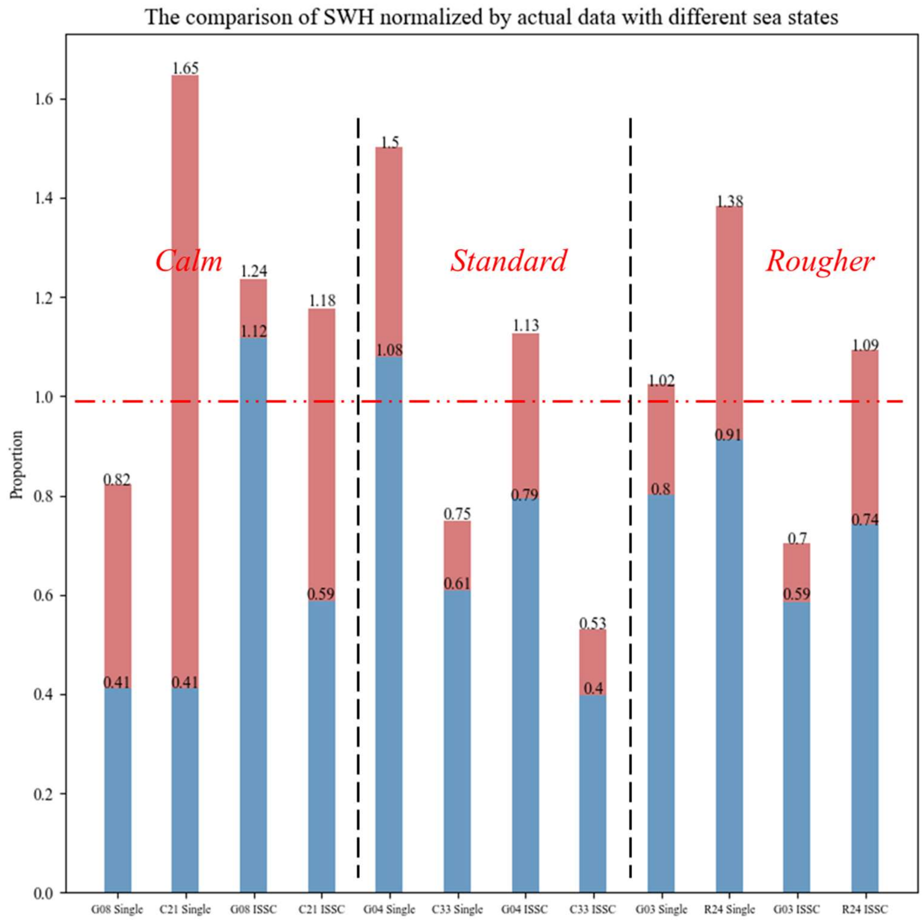

Fig.3.35 The comparison of SWH normalized by actual data with different sea states

In Fig.3.35, SWH estimated is normalized by actual data with different sea states based on the Fig.3.34. The performance of single-frequency wave model is better than the multi-frequency wave model with ISSC Spectrum. The ISSC Spectrum for simulation might be not suitable for the Tsushima strait. But whether it is a single-frequency wave model or a multi-frequency wave model with ISSC Spectrum, the fundamental pattern of Number Crossing and SWH, which is the more numbers crossing, the larger SWH becomes, is proved.

CHAPTER 4: Discussion and Conclusion

4.1 Discussion

Here are some factors that need to be discussed in this research.

(1) A limitation of sampling frequency in Fig.3.5, is found and it can be explained that the wave height becomes larger, and the frequency of the high-frequency variation also increases. According to Nyquist, the sampling frequency should be twice the maximum frequency in the signal. If not, that will cause aliasing. In this research, the sampling frequency of the data recorded is 20Hz and if we use a higher sampling frequency like 40Hz, the limitation will change. In Fig.4.1, the new limitation point in red is delayed concerning the old one.

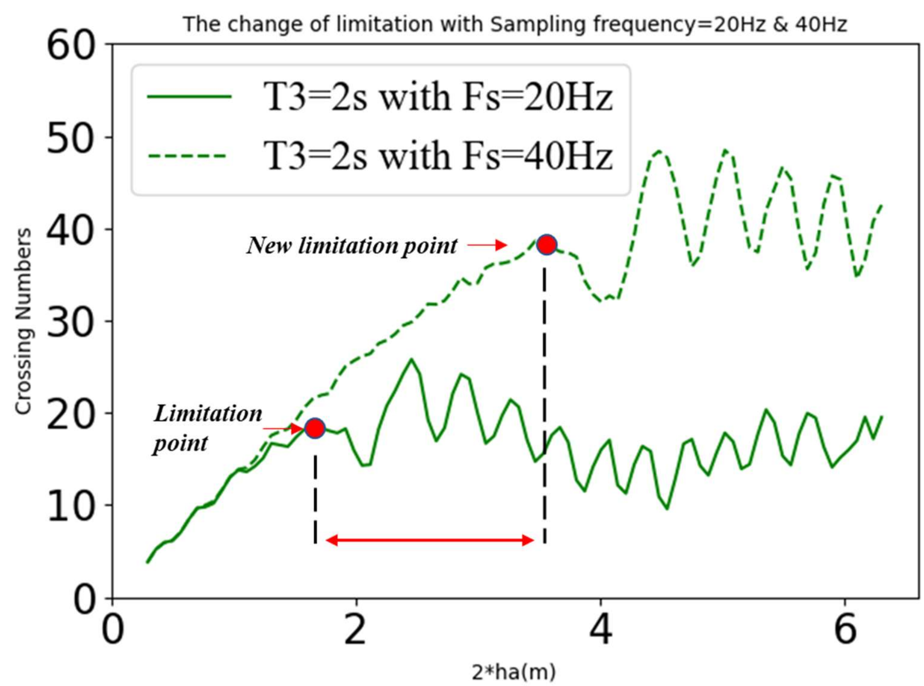

Fig.4.1 The change of limitation with Sampling frequency 20Hz & 40Hz

(2) The SNR resolution is also a factor that can't be ignored. The SNR resolution of the actual data is only 1db, called truncated SNR, but the data in the simulation is continuous. The differences between continuous SNR data and truncated SNR data are shown in Fig.4.2. With using truncated SNR, there is almost no change in range A, and a sharp increase appears in range B. We may lose some details in the data we received because we couldn't record the change of SNR which is in the range from 0db to 1db.

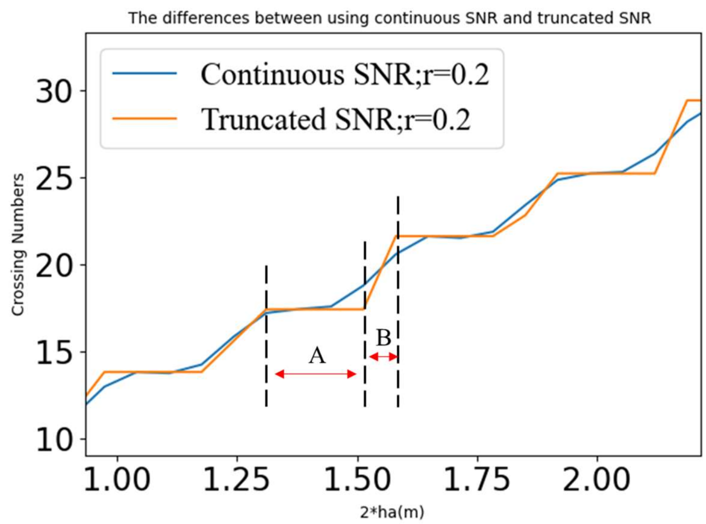

Fig.4.2 The differences between using continuous SNR and truncated SNR

(3) The ship motions should be considered when measuring. As the ship motion is impacted by the main engine, plus the wind, the waves, and the currents. Although these movements can be subtle, they also could be recorded as periodic noise we don't want. In this research, the antenna is set on the right-hand side of the front part of the ship. So the main way of the ship motion could be the pitch and roll. Generally, the ship motion has a longer wave period and smaller amplitude in the signal. The certain values of number crossing corresponding to the SWH in the look-up table might be a little different with different ship motions, but the fundamental pattern of number crossing and

SWH would not change.

(4) There are some of the Spectrum models for simulation could be chosen, such as the Gaussian swell spectrum and the JONSWAP spectrum. In Fig.4.3, it is shown that the results of the Gaussian swell spectrum and ISSC spectrum are different. And That should depend on the observation area. The ISSC spectrum might not be suitable for the Tsushima strait because the range of low frequency shown in Fig.3.11 is quite a bit large, meaning lots of waves of long wave periods are included. In fact, there is almost no swell in the Tsushima strait. The spectrum model of simulation in the Tsushima strait should be sharper than the ISSC spectrum.

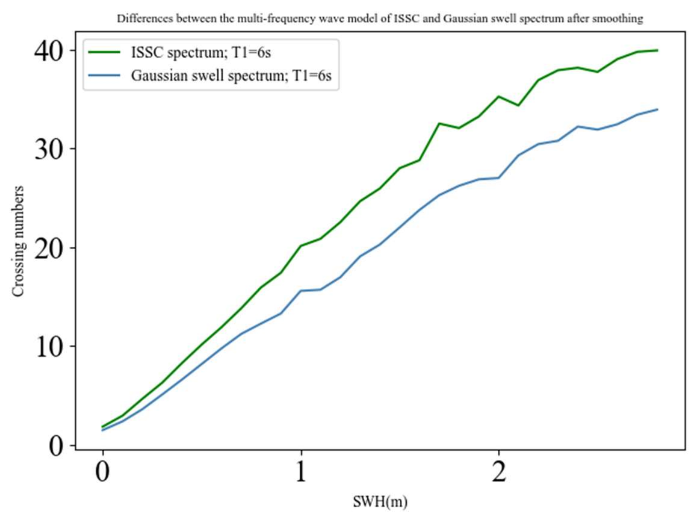

Fig.4.3 The differences between ISSC Spectrum and Gaussian swell spectrum

(5) The duration of the data we use should be discussed. As the comparison in Fig 4.4 and Fig 4.5 and 4.6, we can see the results of ACF are bad when the peak wave period we set over around 4s with 2 min data. Therefore, the accuracy of wave period estimation in rougher sea states as shown in Fig 3.33 and Fig 3.34 is bad. We could use longer data to determine the wave period estimation with ACF in future work.

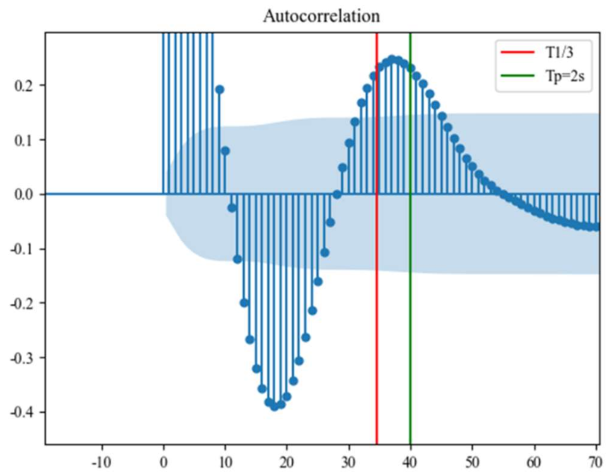

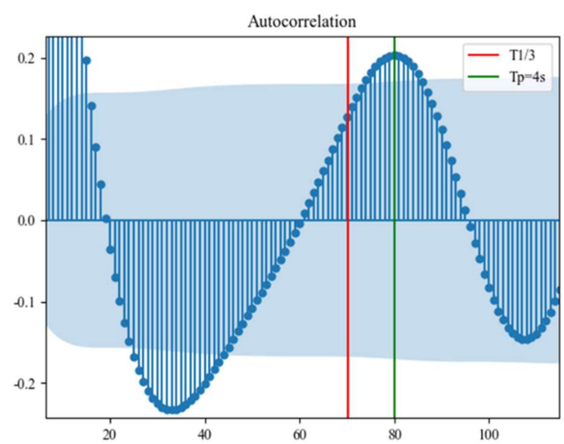

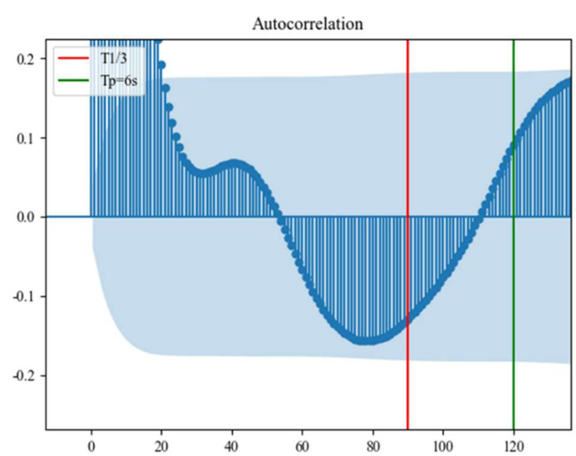

Fig 4.4, 4.5 and 4.6 The result of ACF with different wave periods simulated

4.2 Conclusion

In this research, the measurement for significant wave height and its period with GNSS-IR on shipborne is introduced. It has the advantages of wide coverage and good observation frequency. The theory is based on the GNSS-IR and the information of the SWH is hidden in the SNR signal. According to the SNR pattern, it enables to make the observations for the changes of SWH with time series at the way of counting the number crossing. In the part of the simulation, the single-frequency wave, and the multi-frequency wave model with ISSC Spectrum are introduced. In the part of results, the results of two models in three kinds of sea states of the Tsushima strait are shown. After comparing them with actual data from the calibration systems (Polaris Hindcast), they are consistent with the fundamental pattern. It can be proved that the more numbers crossing, the larger SWH estimated with a rougher sea state. But ISSC Spectrum maybe is not suitable for Tsushima Strait.

In future work, the improvements of increasing the range of elevation angles over which data can be received by receivers, developing suitable spectrum models for different observation areas, and a better method and longer data for wave period estimation should be considered.

Reference:

[1] Kinsman, Blair (1984), Wind waves: their generation and propagation on the ocean surface, Dover Publications, ISBN 0-486-49511-6

[2] "About earth:: A global map of wind, weather, and ocean conditions"

[3] RIBOT M A, KUCWAJ J C, BOTTERON C, et al.Normalized GNSS interference pattern technique for altimetry[J]. Sensors (basel),2014,14(6):10234-10257.DOI: 10.3390/s140610234

[4] Martín-Neira M. A passive reflectometry and interferometry system (PARIS) application to ocean altimetry[J].ESA Journal,1993, 17(4):331-335

[5] Stephen, J., & Garrison, J.L. (1996). Utilizing GPS To Determine Ionospheric Delay Over the Ocean.

[6] M. Martin-Neira, M. Caparrini, J. Font-Rossello, S. Lannelongue and C. S. Vallmitjana, "The PARIS concept: an experimental demonstration of sea surface altimetry using GPS reflected signals," in IEEE Transactions on Geoscience and Remote Sensing, vol. 39, no. 1, pp. 142-150, Jan. 2001, doi: 10.1109/36.898676.

[7] Martín-Neira, Manuel et al. “Altimetry precision of 1 cm over a pond using the wide-lane carrier phase of GPS reflected signals.” Canadian Journal of Remote Sensing 28 (2002): 394 - 403.

[8] Lowe, Stephen T. et al. “An ocean-altimetry measurement using reflected GPS signals observed from a low-altitude aircraft.” IGARSS 2000. IEEE 2000 International Geoscience and Remote Sensing Symposium. Taking the Pulse of the Planet: The Role of Remote Sensing in Managing the Environment. Proceedings (Cat. No.00CH37120) 5 (2000): 2185-2187 vol.5.

[9] Garrison, James L. et al. “Wind speed measurement using forward scattered GPS signals.” IEEE Trans. Geosci. Remote. Sens. 40 (2002): 50-65.

[10] Lin, Bing et al. “Relationship between GPS signals reflected from sea surfaces and surface winds: Modeling results and comparisons with aircraft measurements.” Journal of Geophysical Research 104 (1999): 20713-20727.

[11] Helm, Achim. “Ground-based GPS altimetry with the L1 OpenGPS receiver using carrier phase delay observations of reflected GPS signals.” (2008).

[12] Kucwaj, Jan et al. “Accurate Pseudorange Estimation by Means of Code and Phase Delay Integration: Application to GNSS-R Altimetry.” IEEE Journal of Selected Topics in Applied Earth Observations and Remote Sensing 9 (2016): 4854-4864.

[13] Liu, Wei et al. “Coastal Sea-Level Measurements Based on GNSS-R Phase Altimetry: A Case Study at the Onsala Space Observatory, Sweden.” IEEE Transactions on Geoscience and Remote Sensing 55 (2017): 5625-5636.

[14] Kucwaj, Jan et al. “Circular Regression Applied to GNSS-R Phase Altimetry.” Remote. Sens. 9 (2017): 651.

[15] Lowe, Stephen T. et al. “5-cm-Precision aircraft ocean altimetry using GPS reflections.” Geophysical Research Letters 29 (2002): n. pag.

[16] Ruffini, Giulio et al. “The Eddy Experiment: Accurate GNSS-R ocean altimetry from low altitude aircraft.” Geophysical Research Letters 31 (2004): n. pag.

[17] Mashburn, Jake et al. “An Assessment of the Precision and Accuracy of Altimetry Retrievals for a Monterey Bay GNSS-R Experiment.” IEEE Journal of Selected Topics in Applied Earth

Observations and Remote Sensing 9 (2016): 4660-4668.

[18] Cardellach, Estel et al. “Consolidating the Precision of Interferometric GNSS-R Ocean Altimetry Using Airborne Experimental Data.” IEEE Transactions on Geoscience and Remote Sensing 52 (2014): 4992-5004.

[19] Carreno-Luengo, Hugo et al. “Experimental Evaluation of GNSS-Reflectometry Altimetric Precision Using the P(Y) and C/A Signals.” IEEE Journal of Selected Topics in Applied Earth Observations and Remote Sensing 7 (2014): 1493-1500.

[20] Martín-Neira, Manuel et al. “The PARIS Ocean Altimeter In-Orbit Demonstrator.” IEEE Transactions on Geoscience and Remote Sensing 49 (2011): 2209-2237.

[21] Park, Hyuk et al. “Retracking considerations in spaceborne GNSS-R altimetry.” GPS Solutions 16 (2012): 507-518.

[22] Pascual, Daniel et al. “Precision Bounds in GNSS-R Ocean Altimetry.” IEEE Journal of Selected Topics in Applied Earth Observations and Remote Sensing 7 (2014): 1416-1423.

[23] D'addio, S. et al. “GNSS-R Altimeter Based on Doppler Multi-looking.” IEEE Journal of Selected Topics in Applied Earth Observations and Remote Sensing 7 (2014): 1452-1460.

[24] Carreno-Luengo, Hugo et al. “3Cat-2: A P(Y) and C/A GNSS-R experimental nano-satellite mission.” 2013 IEEE International Geoscience and Remote Sensing Symposium - IGARSS (2013): 843-846.

[25] Santamaría-Gómez, Alvaro et al. “Levelling co-located GNSS and tide gauge stations using GNSS reflectometry.” Journal of Geodesy 89 (2015): 241-258.

[26] Roussel, Nicolas et al. “Sea level monitoring and sea state estimate using a single geodetic

receiver." Remote Sensing of Environment 171 (2015): 261-277.

[27] Jin, Shuanggen et al. "Sea level change from BeiDou Navigation Satellite System-Reflectometry (BDS-R): First results and evaluation." Global and Planetary Change 149 (2017): 20-25.

[28] Georgiadou, Paraskevi and Alfred Kleusberg. "On carrier signal multipath effects in relative GPS positioning." (1988).

[29] GNSS 反射信号海洋遥感方法及应用/ 杨凯东,王峰著.-北京：科学出版社，2020.3

[30] 吴夏平, 王福明. 基于最小二乘法原理的趋势项处理研究 [J]. 微计算机信息, 2008, 24(30): 254-255.

[31] Tucker M J, 1991. Waves in Ocean Engineering. Ellis Horwood Ltd. (Chichester).